Evidence for Fine-grained Material at Lunar Red Spots: Insights from Thermal Infrared and Radar Data Sets

Benjamin D Byron[1] , Catherine M. Elder[1] , Timothy D. Glotch[2] , Paul O. Hayne[3] , Lori M. Pigue[4], and Joshua T. S. Cahill[2,5]

[1] Jet Propulsion Laboratory, California Institute of Technology, 4800 Oak Grove Drive, Pasadena, CA 91109, USA; benjamin.d.byron@jpl.nasa.gov

[2] Stony Brook University, 100 Nicolls Road, Stony Brook, NY 11794, USA

[3] Laboratory for Atmospheric and Space Physics, University of Colorado, 1234 Innovation Drive, Boulder, CO 80303, USA

[4] U.S. Geological Survey, Astrogeology Science Center, 2255 N. Gemini Drive, Flagstaff, AZ 86001, USA

[5] Johns Hopkins University Applied Physics Laboratory, 11100 Johns Hopkins Road, Laurel, MD 20723, USA

Abstract

Lunar red spots are small spectrally red features that have been proposed to be the result of non-mare volcanism. Studies have shown that a number of red spots are silicic, and are spectrally distinct from both highlands and mare compositions. In this work, we use data from LRO Diviner, Mini-RF, and Arecibo to investigate the material properties of 10 red spots. We create albedo maps using Diviner daytime solar reflectance data to use as an input to our improved thermophysical model, and calculate the rock abundance (RA) and H-parameter values that best fit Diviner nighttime thermal infrared radiance measurements. The H-parameter can be considered analogous to the thermal inertia of the regolith, with a high H-parameter corresponding to low thermal inertia. We find that the red spots generally have low RA, and do not have a uniform H-parameter but contain localized regions of high H-parameter. We additionally find that the red spots have a low circular polarization ratio (CPR) in many of the same locations that show a low RA and high H-parameter. Low RA, high H-parameter, and low CPR indicate a relative lack of rocks larger than ~ 10 cm, which is consistent with previous findings of a mantling of fine-grained pyroclastic material for at least three red spots. Areas with high H-parameter but that do not show clear signs of pyroclastics in other data sets may be evidence of previously undiscovered pyroclastics, or could be due to the unique physical properties (e.g., porosity, rock strength/breakdown resistance) of the rocks that make up the red spots.

Unified Astronomy Thesaurus concepts: Lunar domes (950); Lunar regolith (2315); Lunar surface (974); Lunar science (972); Remote sensing (2191); Radar observations (2287)

1. Introduction

The majority of lunar volcanic activity is associated with the maria, the large basaltic plains that cover much of the lunar nearside. However, throughout the lunar maria there are anomalous spectral features (called "red spots") that are suggested to be the result of non-mare volcanism. These features are spectrally red, meaning that they are highly absorptive in the ultraviolet (UV) and highly reflective at increasingly longer visible and near-infrared wavelengths (Whitaker 1972; Head & McCord 1978). Their red color can be observed in UV/visible color-ratio maps from the Clementine mission (Figure 1; McEwen & Robinson 1997). Some examples of lunar red spots include Mons Hansteen, the Gruithuisen domes, Lassell Massif, the Darney and Helmet features, and the Compton–Belkovich Volcanic Complex (CBVC).

Red spots occur in a variety of geologic settings, associated with domes, smooth plains, and rugged patches of highlands material, and are generally found in the nearside Procellarum Potassium, Rare Earth Elements, and Phosphorous (KREEP) Terrane (Wood & Head 1975). CBVC is the exception to this, as it is located on the lunar farside near an isolated thorium anomaly (Jolliff et al. 2011). Some red spots make up part of the Imbrium basin inner ring (Mons La Hire, Mons

Spitzbergen), indicating that the red material was present prior to the Imbrium impact and subsequently uplifted during the impact event. Others are associated with ejecta from impact craters in the Imbrium region (e.g., Copernicus, Archimedes, and Plato craters), representing red material that has been excavated from beneath the mare basalts (Wood & Head 1975), while others appear to be the product of post-Imbrium but pre-mare extrusive volcanism (Gruithuisen domes, Mairan domes, Mons Hansteen; Wood & Head 1975; Head & McCord 1978). Many of the red spots that are found in the southern Procellarum KREEP Terrane (e.g., Darney-chi and -tau, Helmet, southern Montes Riphaeus) occur as patches of smooth plains or as sections of basin rim structures related to Mare Cognitum and Mare Humorum (Wood & Head 1975).

The steep-sided morphology of the red spot domes (e.g., Gruithuisen domes, Mairan domes, and Mons Hansteen) is similar to that of terrestrial silicic volcanic domes, suggesting that they were formed by the eruption of highly viscous lavas with lower extrusion rates than mare basalts (Head et al. 1978). Many of the red spots in the Procellarum KREEP Terrane appear to be embayed by mare material, indicating that they were emplaced prior to the eruption of the surrounding mare (Wood & Head 1975). Crater-counting methods support this, with age estimates of red spots finding that they predate most mare deposits (Wagner et al. 2002, 2010; Ashley et al. 2016). The fact that the red spots are embayed by younger mare material also suggests that they may have covered a larger area of the lunar surface in the past before being covered by mare lavas. Materials that are spectrally similar to red spots have also

been exposed by impact craters, supporting the presence of intrusive or buried non-mare volcanic material on the Moon (Glotch et al. 2010; Shkuratov et al. 2016; Glotch et al. 2021).

In addition to the strong UV absorption, red spots are also associated with low FeO and TiO_2 abundances, and in some cases high thorium content (Hagerty et al. 2006). These compositional findings, in conjunction with the morphologic studies (Head et al. 1978), further support the hypothesis that at least some of the red spot features are the result of non-mare volcanism. Additional studies using data from the Diviner Lunar Radiometer Experiment (Diviner) on the Lunar Reconnaissance Orbiter (LRO) found evidence for silica-rich material at a number of red spots (Glotch et al. 2010, 2011; Jolliff et al. 2011), determining that some of the red spots (Gruithuisen domes, Mons Hansteen, Lassell Massif, Mairan domes, and CBVC) have a mid-infrared (mid-IR) spectral shape that is best explained by the presence of highly silicic materials such as quartz, silica-rich glass, or alkali feldspar. Other prominent red spots (e.g., Helmet, Darney-chi and -tau, and southern Montes Riphaeus) have low FeO and TiO_2 abundance but are not consistent with silicic composition and do not display a thorium anomaly (Hagerty et al. 2006; Glotch et al. 2010).

Gravity modeling techniques using observations from the Gravity Recovery and Interior Laboratory (GRAIL) mission provided further constraints on the composition of lunar red spots. Kiefer et al. (2016) used GRAIL free-air gravity data in conjunction with a model to derive bulk crustal density values for the Gruithuisen domes and Mons Hansteen. The study found that the derived crustal densities (2150 kg/m3 for the Gruithuisen Delta dome and 1500–2000 kg/m3 for Mons Hansteen) were lower than the density of both mare basalts (>3000 kg/m3) and felsic highlands material (2350–2450 kg/m3). Kiefer et al. (2016) therefore invoked lower-density volcanic glass or an additional large-scale porosity due to vesicularity or pyroclastics in order to explain the low densities, and concluded that the volcanic domes contain an abundance of low-density felsic material.

Three primary mechanisms have been proposed to explain the formation of low-density, thorium-rich, silicic volcanic material that coincides with many of the red spots. The first is silicate liquid immiscibility (SLI), which occurs when a basaltic magma undergoes extensive fractional crystallization and the residual magma separates into two immiscible melts. One of the melts would then be SiO_2-poor and FeO-rich, while the other would be SiO_2-rich and FeO-poor (Hess et al. 1975). Immiscible melts have been discovered on the microscopic scale in returned Apollo samples (Roedder & Weiblen 1970; Roedder & Weiblen 1971; Roedder & Weiblen 1972), and experimental studies have found that the FeO and SiO_2 contents of the SiO_2-rich melt resulting from SLI were similar to that of the Gruithuisen domes as measured by Diviner (Kusuma et al. 2012), suggesting that SLI is a viable mechanism for producing the highly silicic compositions on the Moon (Roy et al. 2023). However, SLI is not expected to result in the large volumes of silicic magma needed to produce the large volcanic domes such as those at Gruithuisen (Hagerty et al. 2006). Additionally, experiments have shown that the mafic component of the SLI would be preferentially enriched in thorium while the felsic component would be thorium-depleted (Neal & Taylor 1989; Gullikson et al. 2016), which is contrary to what is observed at the felsic and thorium-rich red spots. Gullikson et al. (2016) argued that for lunar granites to have

formed by SLI, a complementary Th- and Fe-rich reservoir must also exist, and the absence of such a reservoir on the Moon indicates that the red spots did not form by SLI. However, Roy et al. (2023) argued that the complementary Fe-rich melt would sink due to its higher density compared with the Si-rich melt, which would explain the absence of the Th- and Fe-rich reservoirs.

Basaltic underplating is another proposed mechanism for the production of silicic magmas on the Moon. This process involves the intrusion of basaltic magma into the lunar crust, leading to partial melting of the crust and the creation of highly silicic and in some cases thorium-rich magmas (Hildreth 1981). Gullikson et al. (2016) suggested that both monzogabbro and alkali gabbronorite (rocks that have a relatively high concentration of alkali and incompatible trace elements) could have made up part of the lunar crust, which subsequently partially melted to form silicic crustal melts. These magmas would be less dense than the surrounding crust, causing the magma to ascend and erupt as silica-rich lava. The basaltic underplating hypothesis is consistent with the age and location of red spots such as Mons Hansteen and the Gruithuisen domes, which were emplaced prior to surrounding mare basalts and near the edges of impact basins (where the thinned lithosphere and extensive fractures provide conduits for magma ascent). Additionally, thermodynamic modeling results show that partial melting (10%–20%) of lunar crustal lithologies can result in the SiO_2 and thorium contents observed at lunar red spots (Ravi et al. 2020), suggesting that underplating is a plausible mechanism for their formation. Ravi et al. (2020) also found that the alkali content (Na_2O wt.% + K_2O wt.%) of the model silicic melt (~0.5–1.0 wt.%) is lower than that of returned silicic fragments from existing Apollo samples (~6.1–8.5 wt.%), though it is unclear if the silicic fragments are representative of the silicic red spot landforms.

The last proposed mechanism is the fractional crystallization of KREEP basalts. Previous tests of the fractional crystallization hypothesis found that a monzogabbro protolith produced 40% melt at 1000 °C with intermediate (56 wt.%) SiO_2, which is inconsistent with the returned Apollo samples (Gullikson et al. 2016). However, thermodynamic modeling showed that >70% fractional crystallization of KREEP basalts resulted in silicic melts with similar SiO_2 (>68 wt.%), alkali (>6.0 wt.%), and thorium contents expected for silicic magma based on returned Apollo samples (Ravi et al. 2022). This suggests that, if the returned silicic fragments are representative of the red spots, KREEP basalts were likely protoliths for the eventual silicic magmas that formed the red spots.

The uncertainty regarding the mechanism of their formation makes red spots a prime location for future lunar landed missions, such as the upcoming Commercial Lunar Payload Services (CLPS) Lunar Vulkan Imaging and Spectroscopy Explorer (Lunar-VISE) payload delivery that will land on one of the Gruithuisen domes.

Here, we present rock abundance and H-parameter maps for the Gruithuisen domes and nine other red spots using thermal infrared data from the Diviner instrument, providing insight into their thermophysical properties in preparation for future missions. Additionally, we make use of radar data sets from both LRO and Earth-based observations to compare with Diviner thermophysical results. Finally, we use these data sets to constrain the unique material properties of the red spots, focusing on the extrusive volcanic structures (i.e., Gruithuisen

Table 1
List of Red Spots Investigated in This Study

Red Spot	Lon/Lat	Age (Ga)	Geologic Context	Reference
Gruithuisen Domes	40.2 W, 36.2 N	3.80	Silicic Domes	Ivanov et al. (2016)
Mairan Domes	47.7 W, 41.4 N	3.75–3.35	Silicic Domes	Boyce et al. (2018)
Mons La Hire	25.5 W, 27.6 N	3.85	Imbrium Basin Ring Structure	Wood & Head (1975)
Montes Spitzbergen	5.0 W, 34.7 N	3.85	Imbrium Basin Ring Structure	Wood & Head (1975)
Helmet	31.5 W, 16.7 S	3.80	Pre-Mare Highlands	Wagner et al. (2010)
Darney-chi and -tau	26.3 W, 11.6 S	3.94	Pre-Mare Highlands	Wagner et al. (2010)
Southern Montes Riphaeus	28.0 W, 9.0 S	N/A	Cognitum Basin Rim Structure	Wagner et al. (2010)
Mons Hansteen	50.3 W, 12.1 S	3.80	Silicic Dome	Qiu et al. (2022)
Lassell Massif	9.1 W, 14.6 S	4.0	Silicic Volcanic Complex	Ashley et al. (2016)
CBVC	99.7 E, 61.2 N	3.50	Silicic Volcanic Complex	Shirley et al. (2016)

domes, Mairan domes, Mons Hansteen, CBVC, and Lassell Massif) and the basin-related structures (Mons La Hire, Montes Spitzbergen, Darney-chi and -tau, Helmet, and southern Montes Riphaeus). For information on the red spots analyzed in this work see Table 1.

2. Background

2.1. Gruithuisen Domes

The Gruithuisen domes are located along the western section of the Imbrium basin rim (40.2° W, 36.2° N), and are composed of two large domes that are roughly elliptical in shape (the western Gamma dome and the eastern Delta dome), and one smaller circular dome called the northwest dome. The steep-sided morphology of the domes suggests they were formed by viscous lava flows, similar to terrestrial silicic domes (Head et al. 1978). Diviner mid-IR emissivity measurements support this finding, showing that the domes display mid-IR spectral shapes consistent with silicic compositions (Glotch et al. 2010). Crater-counting methods estimate ages of ∼3.80 Ga for the Gamma and Delta domes, and surrounding mare units were found to have formed after the domes (Ivanov et al. 2016).

2.2. Mairan Domes

The Mairan domes are located in northern Oceanus Procellarum (∼47.7° E, 41.4° N), and consist of four volcanic domes that have high albedo and strong UV absorption (Head & McCord 1978). Similar to the Gruithuisen domes, their steep-sided morphology suggests that they were formed by non-mare extrusive volcanism (Head et al. 1978), their high Th content (36.5, 48.0, and 82.8 ppm for the "T," "Middle," and "South" domes, respectively; Glotch et al. 2011) is indicative of evolved lavas, and their mid-IR spectral shape suggests that they are silicic in composition (Glotch et al. 2011). The Mairan "Middle" dome was suggested to have been constructed in two phases, the first occurring ∼3.75 Ga and the second ∼3.35 Ga (Boyce et al. 2018). The first phase consisted of lavas with relatively high SiO_2 content (70%–90%; Glotch et al. 2011) and low Fe content (7%–13%; Boyce et al. 2018) that erupted from at least seven small volcanic constructs, and the second consisted of high SiO_2 lavas at the dome summits and moderately lower SiO_2 lavas at the topographically lower central plateau (Boyce et al. 2018). Crater-counting also suggests that the mare surfaces surrounding the domes were emplaced in multiple phases at ∼3.73 and ∼3.35 Ga, roughly concurrent with the silicic domes (Boyce et al. 2018).

2.3. Mons La Hire and Montes Spitzbergen

Mons La Hire (25.5° W, 27.6° N) and Montes Spitzbergen (5° W, 34.7° N) are mountains that make up part of the inner ring of the Imbrium basin. They appear to have been uplifted during the Imbrium basin-forming event, and are likely not volcanic in origin (Wood & Head 1975). The lack of a thorium anomaly (6.9 ppm; Hawke et al. 2003; Hagerty et al. 2006) and the lack of a silicic mid-IR spectral shape (Glotch et al. 2010) indicate that Mons La Hire and Montes Spitzbergen are not silicic in composition.

2.4. Helmet

The Helmet feature is located northeast of Mare Humorum (31.5° W, 16.7° S), contains a light plains unit, a hummocky unit, and two massifs, and is either volcanic in origin or was excavated by the Cognitum basin-forming impact (Wagner et al. 2010). Although it is clearly red in the Clementine color-ratio map (Figure 1), Diviner emissivity spectra do not indicate a silicic composition for the feature (Glotch et al. 2010) and it does not display a thorium anomaly (7.3 ppm; Hagerty et al. 2006). Wagner et al. (2010) derived an absolute model age of ∼3.80 Ga for the light plains unit, and noted that it is embayed by mare materials ranging from 3.40–3.45 Ga.

2.5. Darney

The Darney feature consists of two units, Darney-chi and Darney-tau, located east of the Helmet feature in Mare Cognitum (26.3° W, 11.6° S). Darney-chi is an elliptical light plains unit surrounded by mare, and Darney-tau is a group of low hills. An absolute model age of 3.94 Ga was derived for Darney-chi, indicating that it predates the surrounding mare units by ∼0.4 Ga (Wagner et al. 2010). The Clementine color-ratio map shows that Darney is clearly spectrally red compared with surrounding mare (Figure 1). However, Diviner emissivity spectra show that Darney is not silicic but has similar values to typical highlands material (Glotch et al. 2010). Thorium data show that it also does not contain a thorium anomaly (8.0 ppm; Hagerty et al. 2006).

2.6. Southern Montes Riphaeus

Montes Riphaeus are located on the northwestern edge of Mare Cognitum, and appear to have been excavated by the Cognitum impact event (Wood & Head 1975). The southern part of the mountains (∼28.0° W, 9.0° S) is spectrally red; however, the feature lacks a thorium anomaly (9.0 ppm;
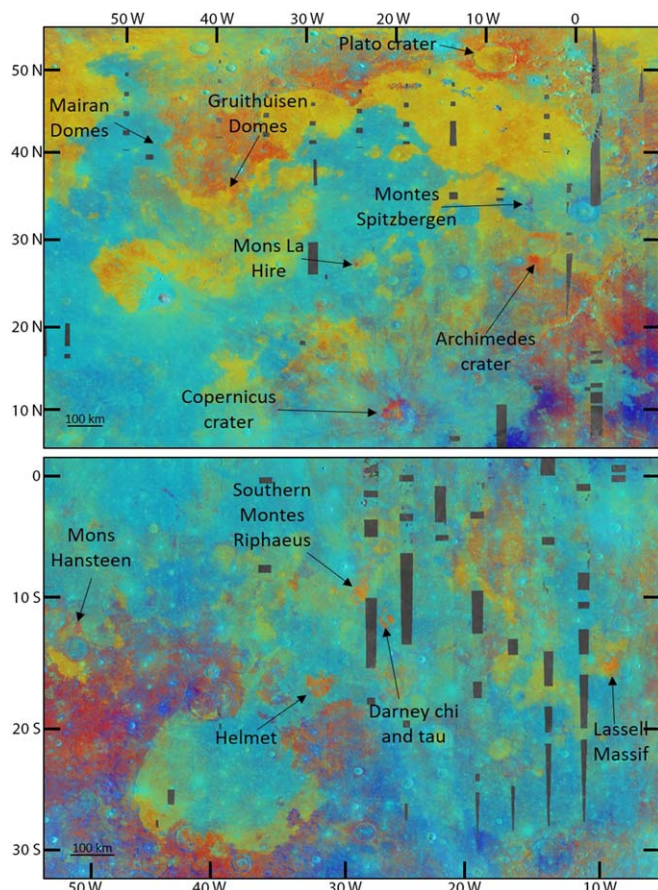
Figure 1. Clementine color-ratio map showing lunar red spots in the vicinity of Mare Imbrium (top) and throughout southern Oceanus Procellarum, Mare Cognitum, and Mare Nubium (bottom). This map was created using three spectral filters (415, 750, and 1000 nm), where red = 750/415, green = 750/1000, and blue = 415/750.

Hagerty et al. 2006) and the mid-IR spectral shape indicates that the location is not silicic (Glotch et al. 2010).

2.7. Mons Hansteen

Mons Hansteen (a.k.a. Hansteen Alpha) is a steep-sided dome in southern Oceanus Procellarum (50.3° W, 12.1° S). The dome contains three distinct geologic units emplaced in three eruption phases (Hilly Dissected Unit, Pitted Unit, and North Massif Unit; Boyce et al. 2017) with absolute model ages ranging from 3.60–3.80 Ga (Qiu et al. 2022), and is embayed by mare material from ~3.0 Ga (Hiesinger et al. 2011). The steep-sided morphology again suggests it was formed by viscous lava flows, and the short Christiansen Feature (CF) locations and mid-IR spectral shape indicate it is silicic in composition (Glotch et al. 2010).

2.8. Lassell Massif

The Lassell Massif is a red spot located in Mare Nubium (9.1° W, 14.6° S). The northern part of the massif is uneven and hummocky, and the southern part of the massif contains two large irregular depressions (Lassell G and K) that may have formed by caldera collapse or explosive venting. The massif and a diffuse area immediately surrounding the southern part of the massif appear red in the Clementine color-ratio map (Figure 1), have short CF values (Glotch et al. 2010), and are

associated with a thorium anomaly (25.0–53.0 ppm; Hagerty et al. 2006), consistent with silicic lithologies. An absolute model age of ~4.0 Ga was found for the northern part of the massif, though Ashley et al. (2016) suggested more recent resurfacing may have occurred at ~900, 400, and 60 Ma due to mass wasting caused by nearby craters or mantling by pyroclastic materials.

2.9. Compton–Belkovich Volcanic Complex

CBVC is the only red spot that is not located in the Procellarum KREEP Terrane. It is composed of a series of volcanic features (including cones, domes, and collapse features) on the lunar farside between the craters Compton and Belkovich (99.7° E, 61.2° N). It was first identified as an isolated thorium anomaly by the Lunar Prospector Gamma Ray Spectrometer instrument (Lawrence et al. 2003). CBVC has generally high reflectance (Clegg-Watkins et al. 2017), displays short CF values (Jolliff et al. 2011), and contains evidence for mantling by fine-grained materials in radar data sets (Bhattacharya et al. 2013; Chauhan et al. 2015). These findings, in conjunction with the existence of the thorium anomaly, all suggest that the CBVC contains silicic pyroclastic materials. An absolute model age of 3.50 Ga was derived for CBVC (Shirley et al. 2016), indicating that it is younger than the red spots found in the nearside maria.

3. Methods

3.1. LRO Diviner

The Diviner Lunar Radiometer Experiment is an infrared and visible radiometer on board LRO (Paige et al. 2010). Diviner has nine channels covering the spectral range 0.3–400 μm, with channels 1 and 2 measuring reflected solar radiation at 0.35–2.8 μm, channels 3–5 measuring thermal emission in the mid-IR (7.55–8.68 μm), and channels 6–9 measuring thermal emission at longer IR wavelengths (13–400 μm). In this work, we primarily utilized nighttime (collected between lunar local time 19:30–05:30) radiance data from Diviner channels 6–8 to investigate the thermophysical properties of the red spots. These data were binned into 128 pixels-per-degree (ppd) spatial resolution and 0.1 lunar hour time resolution. We additionally analyzed Diviner channel 1 daytime solar reflectance data in order to calculate broadband albedo, which we used as an input to our thermal model that we use to derive regolith H-parameter values (see Hayne et al. 2017 and Section 3.1.3 for detailed methods).

3.1.1. Diviner Rock Abundance

We calculated rock abundance (RA) and nighttime regolith temperature from the channels 6–8 nighttime radiance data using the method of Bandfield et al. (2011). This method is based on the principle of anisothermality, in which multiple surface temperatures exist within the Diviner field of view for a given observation. Because rocks have higher thermal inertia than regolith, they stay warmer throughout the lunar night and radiate more at shorter wavelengths (i.e., channels 6 and 7) compared with the cooler regolith, which has a greater radiance contribution at longer wavelengths. The areal fraction of rocks (>~0.5–1 m diameter) within a Diviner pixel can then be estimated by comparing model rock temperatures with the nighttime Diviner multispectral data to find the best-fit rock

abundance and regolith temperature. Regolith temperature in this sense refers to the thermal emission that remains after removing the contribution from the rocks. Bandfield et al. (2011) found that the average global rock concentration was ~0.4%; however, higher rock concentrations (>1%) were seen at fresh impact craters and rilles. We follow the Bandfield et al. (2011) method and create local area RA and regolith temperature maps for each of the red spots, utilizing the additional data collected in the time since the previous RA maps were published on the Planetary Data System (Bandfield et al. 2017). We additionally make use of the updated processing methods that correct angular offset errors in instrument pointing (Powell et al. 2022), which improved the quality of the Diviner data products.

3.1.2. Diviner H-parameter

Using the nighttime regolith temperature maps that were derived simultaneously with RA, it is possible to infer the thermophysical properties (e.g., density, conductivity) of the regolith (Vasavada et al. 2012; Yu & Fa 2016; Hayne et al. 2017; Williams et al. 2017). Vasavada et al. (2012) found that an exponential density profile model provided an improved fit to Diviner nighttime equatorial data over previous models, with the variation in density with depth being described as:

$$\rho(z) = \rho_d - (\rho_d - \rho_s)e^{-z/\mathrm{H}} \tag{1}$$

where ρ_s is the surface density, ρ_d is the density at depth, z is depth, and H is a parameter that controls the change in density with depth. Thermal conductivity, k, depends on density and therefore also varies exponentially with depth in this model. This density profile was used in the 1D heat diffusion model of Hayne & Aharonson (2015) and Hayne et al. (2017), which describes the variation of temperature as a function of time and depth. This model accounts for radiative-conductive heat balance on sunlit surfaces, which are typically close to radiative equilibrium due to the very low thermal inertia of lunar regolith, such that daytime temperatures are primarily controlled by albedo and emissivity. During the lunar nighttime and in shadow, temperatures depend much more sensitively on the thermal conductivity, density, and heat capacity of the regolith.

Hayne et al. (2017) fit the model to the global Diviner nighttime regolith temperature maps of Bandfield et al. (2017) with H as the free parameter, creating a global best-fit H-parameter map. As the H-parameter controls regolith density in this model, and thermal inertia is proportional to $\sqrt{K\rho}$ (where k is assumed to increase linearly with ρ, meaning that thermal inertia is proportional to ρ), H-parameter is considered to be proportional to regolith thermal inertia. The global H-parameter map of Hayne et al. (2017) highlighted the variations in regolith thermal inertia that occur at features such as impact craters and pyroclastic deposits, which appear as high and low thermal inertia, respectively. The average global H-parameter was found to be 0.068 m, and little difference in thermal inertia was seen between the maria and highlands at the global scale (Hayne et al. 2017). We followed the method of Hayne et al. (2017), fitting the regolith temperature maps (derived in the RA calculation described above) to the model using a nonlinear least-squares minimization technique to find the best-fit value for H. As described in the next section, in this

calculation we use albedo data with a higher spatial resolution than that used by Hayne et al. (2017).

3.1.3. Diviner Channel 1 Albedo

Surface albedo influences the diurnal heating and cooling of the surface, and therefore also influences our H-parameter results. A higher albedo surface reflects more sunlight, which results in less heating of the surface during the day and therefore cooler temperatures during the lunar night (Hayne et al. 2017). A higher albedo surface can therefore be mistaken for a higher H-parameter if albedo is improperly accounted for. Previous studies that applied the H-parameter method used the Lunar Orbiter Laser Altimeter (LOLA) 1064 nm normal albedo map, scaled to match Diviner equatorial bolometric solar channel measurements (from Vasavada et al. 2012). The advantage of this method is that the LOLA normal albedo was acquired at zero-degree phase angle, removing any topographic shadowing effects. Scaling the normal albedo to match the Diviner solar channel data ensures that it represents the broadband solar albedo, which is the albedo that controls the heat balance of the lunar surface and is therefore most relevant to the thermal model. However, the relatively low spatial resolution (10 ppd or ~3.0 km pixel^{-1}) of the LOLA albedo map means that some of the finer features of the surface were not entirely resolved in previous work. Because red spots are relatively small (<50 km) features that have a high albedo but are surrounded by low albedo maria, we found that the LOLA albedo map did not adequately resolve the red spots. Therefore, albedo variations could be mistaken for a higher H-parameter. In fact, many red spots appear as high-H regions in the global H-parameter map of Hayne et al. (2017). Here, we use Diviner channel 1 reflectance data, which has a higher spatial resolution (128 ppd) than the previously utilized LOLA albedo map, to calculate albedo and input into our thermal model to generate the H-parameter maps. This ensures that any albedo-related errors are minimized.

Channel 1 of the Diviner instrument is a broadband (0.35–2.8 μm) solar channel that measures solar radiation reflected from the lunar surface. This reflectance product is reported as the radiance relative to a normally illuminated Lambert surface, also known as a radiance factor. We created local area maps of the daytime channel 1 reflectance, collecting data from 09:00 to 15:00 and binning at 128 ppd spatial resolution and 1 hr time resolution. We additionally collected incidence angle data for each of the observations, and then divided the radiance factor by the cosine of the incidence angle to convert it into a Lambert albedo. We averaged the Lambert albedo over all time bins in order to create the final Lambert albedo maps. These local area Lambert albedo maps (Figure 2) were then used as inputs to the thermal model from Hayne & Aharonson (2015) and Hayne et al. (2017), which was used to derive best-fit H-parameter maps for each red spot.

3.1.4. Topographic Correction

Local topography is another factor that must be accounted for in the RA and H-parameter models, as it can cause notable changes in nighttime surface temperature. For example, an equator-facing slope will receive more intense sunlight than a pole-facing slope at a similar latitude, and will therefore experience higher temperatures. Similarly, from the point of view of an east-facing slope, the Sun will rise earlier and set
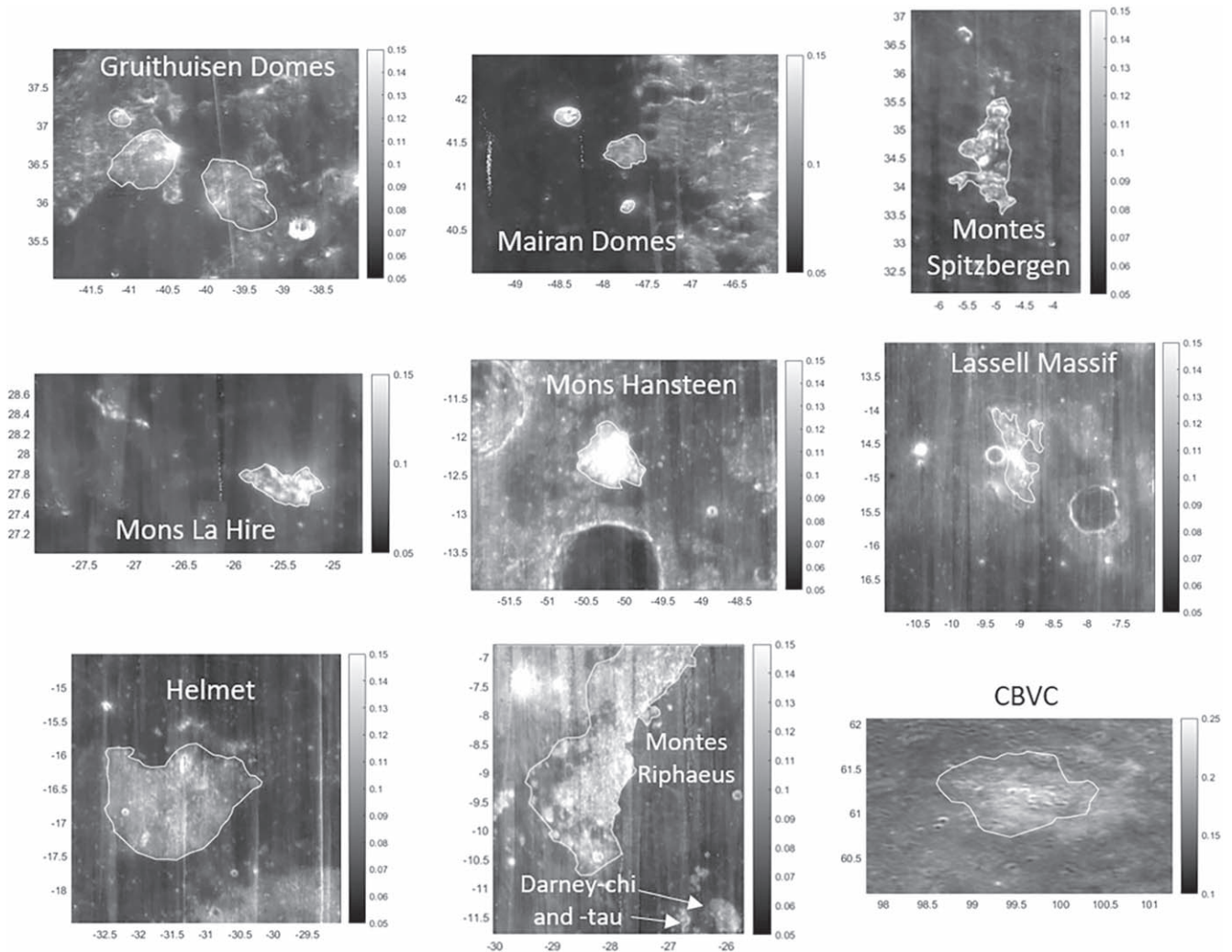
Figure 2. Lambert Albedo maps created using Diviner Channel 1 solar reflectance data. Red spots (outlined in each image) generally have higher reflectance than surrounding maria. We use these albedo maps as an input to our H-parameter model.

earlier than at a west-facing slope. Both of these can be accounted for by correcting the temperatures based on the local slope and azimuth values. Using slope and azimuth maps created from the GLD100 digital elevation model created using LROC Wide Angle Camera (WAC) stereo image data (Scholten et al. 2012), we adjusted the latitude and local times of each pixel in our maps based on the north–south and east–west components of the slope, respectively. The following equations from Hayne et al. (2017) were used to calculate the effective latitude, φ', and effective local time, t':

$$\varphi' = \varphi + \frac{180}{\pi} \tan^{-1}(x \cos \gamma) \tag{2}$$

$$t' = t + \frac{12\,h}{\pi} \tan^{-1}(x \sin \gamma) \tag{3}$$

where x is local slope, and γ is local azimuth angle, and φ and t are uncorrected latitude and local time, respectively.

3.2. Radar Data Sets

3.2.1. LRO Mini-RF and Arecibo

The Miniature Radio Frequency (Mini-RF) instrument on LRO is a synthetic aperture radar that operates in S-band

(12.6 cm) and X-band (4.2 cm) wavelengths (Raney et al. 2010) with a nominal incidence angle of 48°. Mini-RF data were collected in data strips with an effective resolution of 30 m pixel^{-1} while in "zoom mode" and 150 m pixel^{-1} in "baseline mode" at the nominal 50 km LRO orbit (Cahill et al. 2014). The instrument operated by transmitting a circularly polarized signal and then measuring the horizontal and vertical components of the returned signal. From collection of the returned signals, it is possible to calculate the four Stokes parameters, S1–S4, which describe the polarization state of the backscattered signal. Additional parameters can then be determined from these Stokes parameters, including the backscattered power in the same-sense polarization (SC), backscattered power in the opposite-sense polarization (OC), and the ratio of these, otherwise referred to as the circular polarization ratio (CPR). We downloaded individual S-band map-projected calibrated data record files covering each red spot (with the exception of the Mairan domes, Mons La Hire, and Montes Spitzbergen, for which Mini-RF does not have coverage), and used a 3×3 low-pass filter to smooth the CPR data.

We additionally made use of Earth-based S-band (2–4 GHz/ 7.5–15 cm) radar data sets in this work to aid in cases where Mini-RF was unable to collect coverage before its transmitter

malfunctioned. These maps were made from a circularly polarized signal transmitted from the Arecibo Observatory and received at the Green Bank Telescope (Campbell et al. 2010). The spatial resolution of these Earth-based maps is 80 m pixel^{-1}. Earth-based maps were found to have complete coverage of the Gruithuisen domes, Mairan domes, Mons La Hire, Montes Spitzbergen, Mons Hansteen, and Helmet, and partial coverage of the Lassell Massif. For these red spots, we analyzed both Mini-RF and Arecibo maps. However, due to known differences in CPR values between the Mini-RF and Arecibo data sets (Carter et al. 2017), we choose to analyze CPR in a relative sense.

3.2.2. Circular Polarization Ratio

CPR is the ratio of SC to OC, and it depends primarily on surface roughness and the distribution of wavelength-scale scatterers (i.e., rock edges/cracks) in the regolith surface and subsurface (Campbell 2002a). For example, a transmitted signal reflecting off of a smooth, rock-free surface will experience only a single scattering event and return to the detector in the opposite polarization in which it was transmitted (i.e., the OC signal will be higher than SC signal). The CPR for a smooth surface would then be <1. Conversely, a signal interacting with a rough or rocky region of the lunar surface will experience multiple scattering events, meaning more signal will be returned with the same-sense polarization and CPR will be closer to or greater than 1. A number of studies have used CPR to investigate surface and subsurface physical properties on the Moon (e.g., Carter et al. 2009; Campbell 2012; Cahill et al. 2014; Ghent et al. 2016; Nypaver et al. 2021), finding that rocky surfaces such as impact crater ejecta blankets and impact melt deposits have high CPR and that rock-poor surfaces such as pyroclastic deposits display low CPR. In this work we utilize both S1 (total power) and CPR data from Mini-RF and CPR data from Arecibo to investigate the surface and subsurface rock content of the red spots and compare with the Diviner RA and H-parameter results.

4. Results

4.1. Gruithuisen Domes

The Gruithuisen domes have low RA across much of their surfaces except for a few large craters (Figure 3). The surrounding maria contain more rocky craters than the domes, but the intercrater mare plains show relatively low RA. We see relatively high (~0.09–0.10 m) H-parameters at only a few locations on the domes, such as the southwest-facing slope of the Delta dome. On the maria beside the south-facing slope of the Delta dome is a small (~100 m) impact crater surrounded by a region of high H-parameter that is likely a cold spot crater. In the Mini-RF CPR map, the west-facing slopes of the Gamma and Delta domes have high CPR, likely due to incidence angle effects. In the Arecibo CPR map, we see high CPR around the impact craters and in some locations on their slopes, and slightly lower CPR on top of the Gamma dome and in the southern part of the Delta dome.

4.2. Mairan Domes

The maria surrounding the Mairan domes to the west contain a number of rocky craters, which the nearby highlands to the east are noticeably lacking, showing low RA (Figure 4). The

Mairan "T" dome and "South" dome are somewhat rocky (mean RA of 1.10% and 0.94%, respectively), have a similar H-parameter to the surrounding maria (0.055–0.060 m), and contain locations with relatively high (⩾1) CPR. The "Middle" dome, conversely, has low RA (mean RA of 0.45% and lacking small rocky craters) and has a similar H-parameter to the highlands to the east (~0.08 m). The CPR of the "Middle" dome is higher than the nearby highlands, with a number of locations of high CPR (⩾1) near the northern and western parts of the dome.

4.3. Mons La Hire

The south-facing side of Mons La Hire is somewhat rocky (RA of 1.0%–2.0%), in contrast to the north-facing side, which has low (~0.3%) RA (Figure 5). The H-parameter of Mons La Hire is similar to that of the surrounding maria, and is not anomalously high like some of the other red spots (e.g., Gruithuisen and Mairan domes; 0.08–0.10 m). The CPR of Mons La Hire is high (⩾1) across most of the feature, with higher values than most of the surrounding maria.

4.4. Montes Spitzbergen

The Montes Spitzbergen red spot has low RA (~0.3%) and few rocky craters (Figure 6). The H-parameter is not anomalous compared with the surrounding maria, showing typical values (~0.07 m) except at some slopes that show a low H-parameter. Many of the peaks and slopes have relatively high CPR, while the lower-lying areas appear to have lower CPR.

4.5. Helmet

The Helmet feature contains a number of rocky craters, but noticeably fewer than the surrounding maria (Figure 7). The central Hummocky unit appears slightly rockier than the light plains unit that covers most of the eastern and western parts of the feature. This is especially noticeable in the northeastern part of the feature, where there are very few rocky craters, and the regolith has a higher H-parameter (~0.09 m) than at the rest of the red spot. Areas of high CPR can be seen that correspond to the rocky craters and to the two massifs, but much of the feature away from the impact craters has noticeably low CPR.

4.6. Darney-chi and -tau

Darney-chi and -tau both contain fewer rocky craters and have lower RA than surrounding maria (Figure 8), although a few slightly rocky (~1%) craters exist on their surfaces mostly around the edges of the features (e.g., the western part of Darney-chi, the southern part of Darney-tau). In the H-parameter map, a distinction can be seen between the central part of Darney-chi (with relatively lower H-parameter; ~0.07 m) and the northwestern part (with higher H-parameter; ~0.09 m). Similarly, in the Mini-RF map, we see slightly higher CPR values surrounding a number of impact craters in the central part of Darney-chi, while the northern part has low CPR and lacks large impact craters. The central part of Darney-tau also has higher H-parameter and lower CPR than surrounding maria.

4.7. Southern Montes Riphaeus

Southern Montes Riphaeus does not have as many small rocky craters as the surrounding maria, and the central part of the ridge has a slightly higher H-parameter than the rest of the
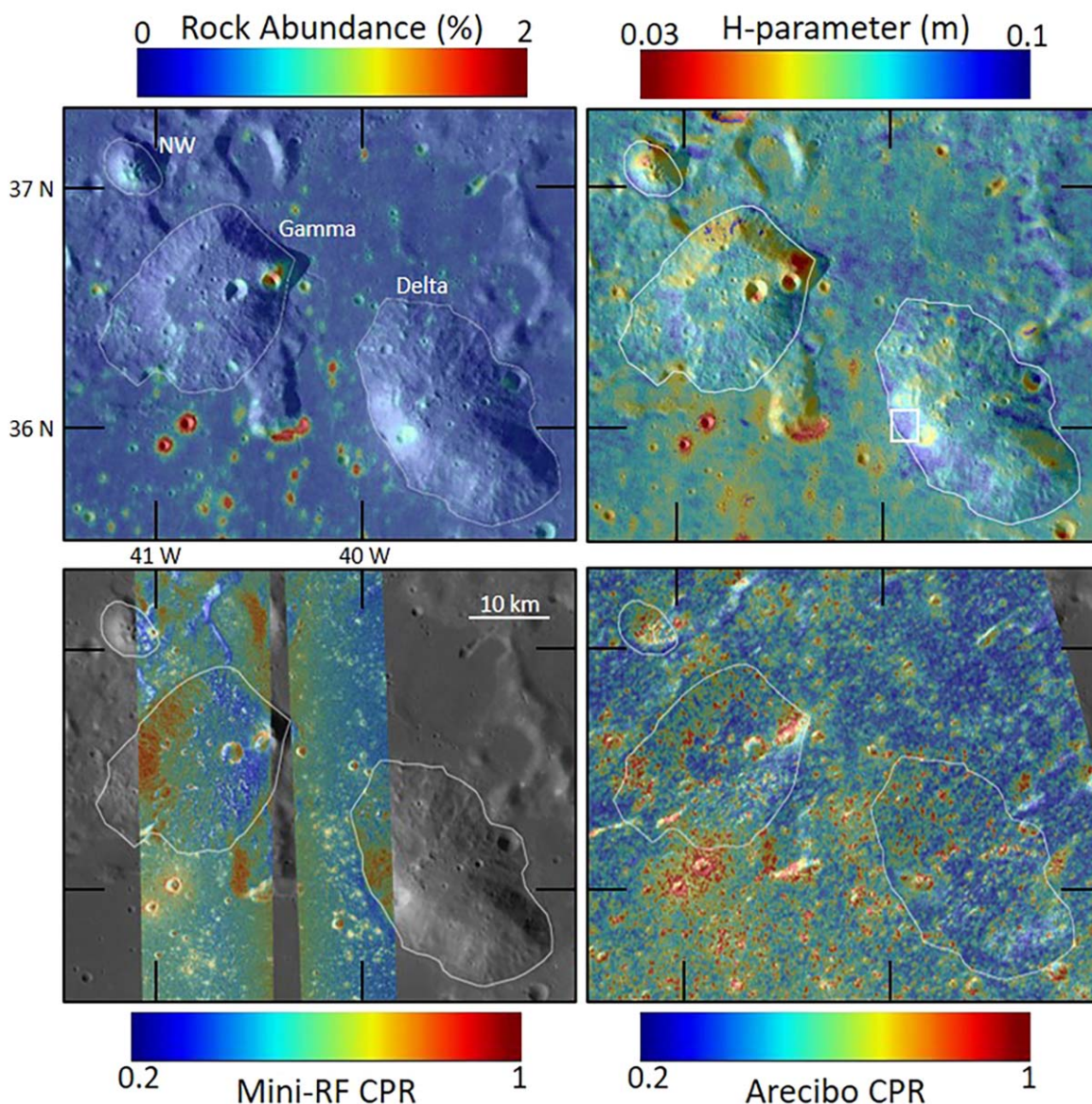
Figure 3. Rock abundance (top left), H-parameter (top right), Mini-RF CPR (bottom left), and Arecibo CPR (bottom right) maps covering the Gruithuisen domes. The white outlines represent the boundaries of the red spot locations determined by our study. The white box in the top-right image is the red spot location analyzed in Figure 15. Note that the color scale for the H-parameter map is inverted. The Diviner maps are overlain on LROC NAC image NAC_ROI_GRUITHSNLO-B_E362N3197_5M. The Mini-RF CPR data are overlain on the S1 total backscatter data. The Arecibo CPR map is overlain on an Arecibo opposite-sense circular polarization image.

feature (Figure 9). The H-parameter of this section is similar to the nearby maria to the southeast, but higher than the maria to the west. Mini-RF has poor coverage over southern Montes Riphaeus; however, we see relatively high CPR values over the very eastern edge of the feature that has coverage.

4.8. Mons Hansteen

At Mons Hansteen, the locations with the highest RA and lowest H-parameter primarily correspond to the Pitted Unit on top of the dome (Figure 10). A small section on the northwest side of the dome and extending outward from the North Massif has slightly lower RA and higher H-parameter than the summit, displaying similar values to surrounding regolith. Similar areas with low RA (0.38%) and relatively higher H-parameter (0.074 m) can be seen in some parts of the Hilly Dissected Unit, although this unit contains some rocky and low H-parameter areas as well.

The Mini-RF and Arecibo CPR maps are similar to the RA and H-parameter maps, generally showing low CPR in areas of low RA and high H-parameter, and showing higher CPR on the Pitted Unit, where RA is high and the H-parameter is low.

4.9. Lassell Massif

The two large irregular craters (Lassell G and K) on the Lassell Massif have high RA, low H-parameter, and high CPR (Figure 11). The hummocky northern part of the massif similarly contains areas of high RA, low H-parameter, and high CPR, and a number of rocky craters are seen in and around the massif. There is a diffuse area surrounding the massif where we see a lack of rocky craters, elevated H-parameter (~0.09–0.10 m), and low CPR relative to the nearby maria. The area with low CPR appears to be generally consistent with the low RA in this area,
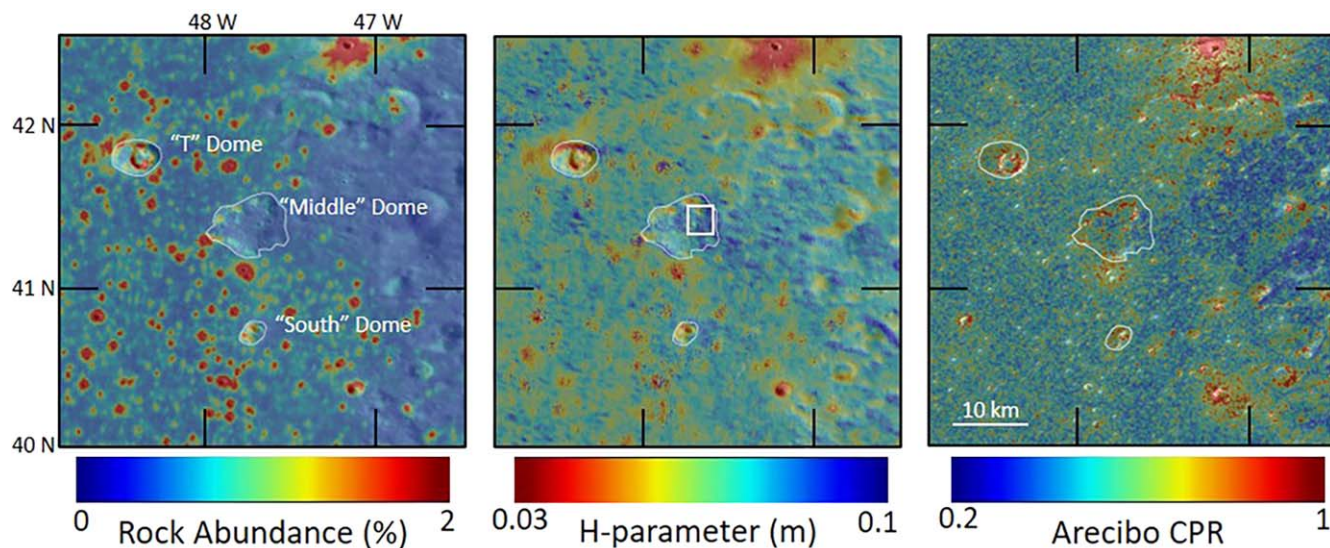
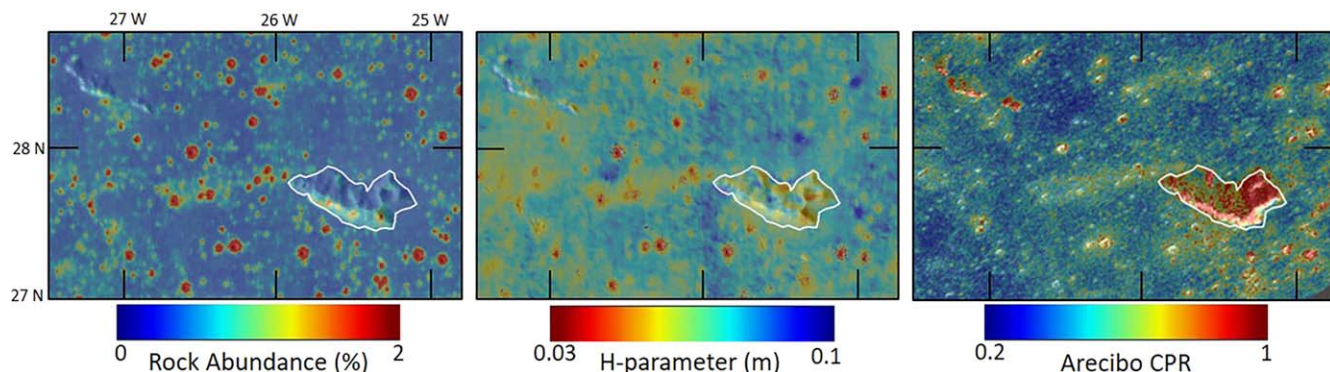**Figure 4.** Rock abundance (left), H-parameter (center), and Arecibo CPR (right) maps covering the Mairan domes. The white outlines represent the boundaries of the red spot locations determined by our study. The white box in the center image is the red spot location analyzed in Figure 15. Note that the color scale for the H-parameter map is inverted. The RA and H-parameter maps are overlain on LROC WAC global mosaic, and the CPR map is overlain on an Arecibo opposite-sense circular polarization image.

Figure 5. Rock abundance (left), H-parameter (center), and Arecibo CPR (right) maps covering Mons La Hire. The white outlines represent the boundaries of the red spot locations determined by our study. Note that the color scale for the H-parameter map is inverted. The RA and H-parameter maps are overlain on an LROC WAC global mosaic, and the CPR map is overlain on an Arecibo opposite-sense circular polarization image.

but extends farther toward the northeast than the high H-parameter does in the Diviner map.

4.10. Compton–Belkovich Volcanic Complex

At CBVC, the areas with highest RA and lowest H-parameter generally correspond to the central caldera, the North dome, and the East dome (Figure 12). However, the majority of the CBVC and the surrounding highlands have low RA. Areas of high H-parameter are seen in a few areas throughout the complex (e.g., west of the central caldera), and the area on the southeastern border of CBVC (east of the East dome along the white line in Figure 12) is seen to be a relatively continuous high H-parameter area. This region also has low CPR as measured by Mini-RF.

4.11. Quantitative Comparison

In Figure 13 we show histograms comparing the RA of pixels within the boundaries of each red spot (i.e., the white polygons in Figures 3–12, and the orange histograms) to all pixels outside the red spots (blue histograms). We see that the Lassell Massif, Helmet, Darney-chi, southern Montes

Riphaeus, and Mons La Hire red spots have slightly lower RA than nearby background maria. The RA values for these red spots peak at ∼0.3%, which is slightly below the global average of 0.4%. The Gruithuisen domes, Mairan domes, Mons Hansteen, CBVC, and Montes Spitzbergen all show similar RA values to surrounding mare (or highlands in the case of CBVC).

Figure 14 shows the corresponding histograms for the H-parameter, with red spots shown in orange and the nearby background shown in blue. Only the Mairan domes and Lassell Massif show a higher H-parameter peak than the background, with most common values for these features being ∼0.08 m. However, all of the red spots (with the exception of Mons Hansteen and Mons La Hire) show a greater frequency of slightly higher H-parameter values than the background maria despite the histogram peaks not always being higher than the nearby background. This means that the red spots generally have a greater number of pixels that have a higher H-parameter compared with the nearby maria. The peaks of the histograms for Mons Hansteen and Mons La Hire have lower H-parameter than nearby maria, with values ∼0.06 m.
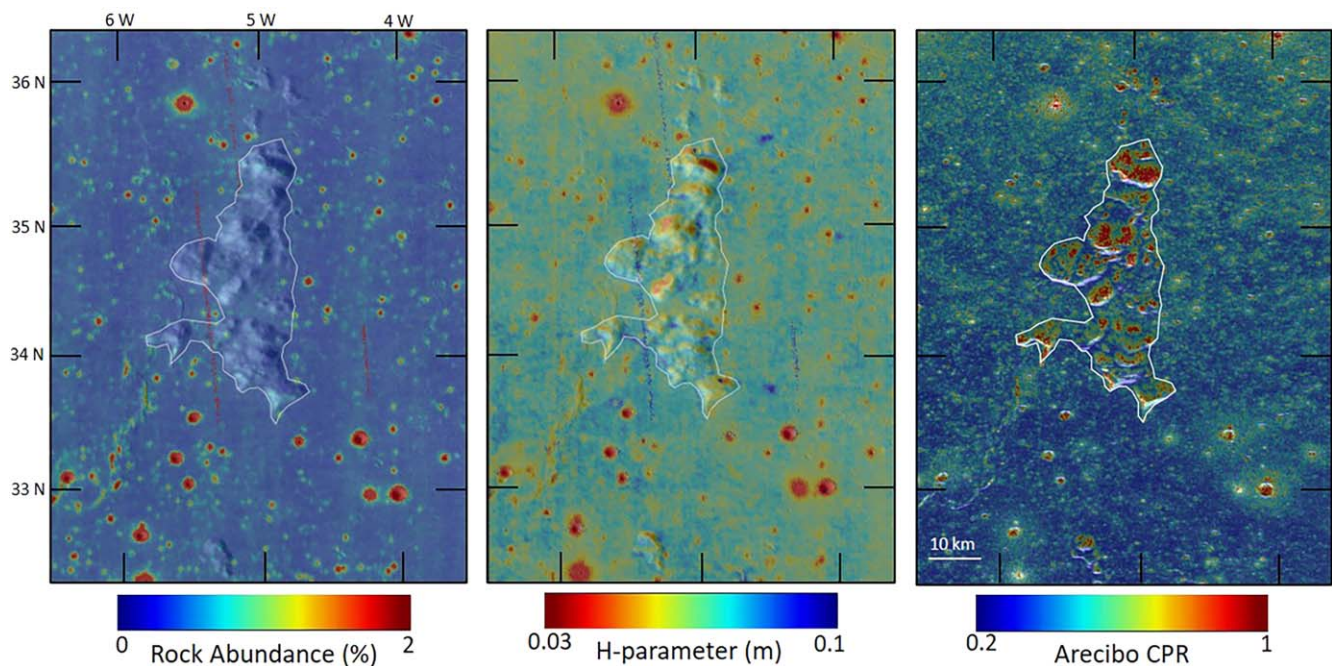
Figure 6. Rock abundance (left), H-parameter (center), and Arecibo CPR (right) maps covering Montes Spitzbergen. The white outlines represent the boundaries of the red spot locations determined by our study. Note that the color scale for the H-parameter map is inverted. The RA and H-parameter maps are overlain on an LROC WAC global mosaic, and the CPR map is overlain on an Arecibo opposite-sense circular polarization image.

Although the red spots do not generally have a uniformly higher H-parameter than their surroundings, we saw that there are localized regions within a number of the red spots (the southern slope of Gruithuisen Delta dome, Mairan "Middle" dome, the northeastern part of Helmet, southern Montes Riphaeus, the northwestern part of Darney-chi, southeastern CBVC, and the area surrounding Lassell G and K) that have a relatively high H-parameter. If we compare the H-parameter values of those selected regions (white boxes in Figures 3, 4, 7, 8, 9, 11, 12) with the nearby background, we see that they are noticeably higher than that of the background (Figure 15).

5. Discussion

5.1. Interpretation of RA, H-Parameter, and CPR

The RA algorithm of Bandfield et al. (2011) that we used in this work is a two-component model that simplifies surface temperatures into a "rock" component (not including buried rocks and rocks <0.5–1 m in diameter, the thermal skin depth of rock on the Moon) and a "regolith" component (fine-grained material where radiative heat transport between grains is important). The rock abundance represents the fraction of the surface covered by the boulders (>~0.5 m in diameter), and the regolith component describes the thermal emission of fine-grained materials at the same location if those boulders were removed. In reality, a given region of the lunar surface is likely to contain both surface and subsurface rocks, as well as a distribution of particle sizes including numerous rocks smaller than 0.5 m but larger than typical regolith fines. The nighttime regolith temperature used in the H-parameter calculation is likely higher than its true value due to buried and/or small rocks (<0.5 m in diameter) cooling faster than the modeled rock component but remaining warmer than the regolith. Such a scenario is predicted for rocky areas, where a range of rock sizes are expected (Bandfield et al. 2011; Hayne et al. 2017). This is supported by the finding that CPR values remain high in

crater ejecta blankets for >3 Ga, which suggests that radar-detectable (i.e., >~10 cm) rocks persist in the near-subsurface even if the surface appears relatively rock-free in Diviner RA measurements (Ghent et al. 2016; Nypaver et al. 2021).

The H-parameter in the model captures how the density and thermal conductivity of the fine-grained regolith component increase with depth (Equation (1)). A lower H-parameter value means that the density of the regolith increases more quickly with depth than for a higher H-parameter. The Hayne et al. (2017) model assumes that thermal conductivity is linearly proportional to density. Therefore, thermal inertia is also proportional to density (see Section 3.1.3), and within the diurnal skin depth (~10 cm) can be considered roughly equivalent to the H-parameter (with a high H-parameter corresponding to low thermal inertia). Fundamentally, thermal inertia is a property that describes how resistant a material is to changes in temperature. On the Moon, the thermal inertia of the fines component is primarily affected by the regolith packing density, but as described previously can also be affected by the presence of small rocks (<0.5–1 m) on the surface or within the diurnal skin depth (Elder et al. 2017; Hayne et al. 2017). A region containing abundant small rocks or subsurface rocks would show higher regolith thermal inertia than a truly rock-free area due to the higher thermal inertia of the rocks. As the small/subsurface rocks break down and comminute into smaller particles over time, the thermal inertia would decrease (Hayne et al. 2017). Areas that contain more fine-grained material at the time of emplacement (e.g., pyroclastic deposits) would have relatively lower thermal inertia (higher H-parameter) in part due to the absence of smaller rocks mixed in with the fines component.

Radar returns from Mini-RF and Earth-based data sets are affected by the presence of wavelength-scale surface and subsurface scatterers (i.e., rocks), and prove complementary to the Diviner thermal IR data sets. A region that contains abundant rocks would have higher CPR due to the greater
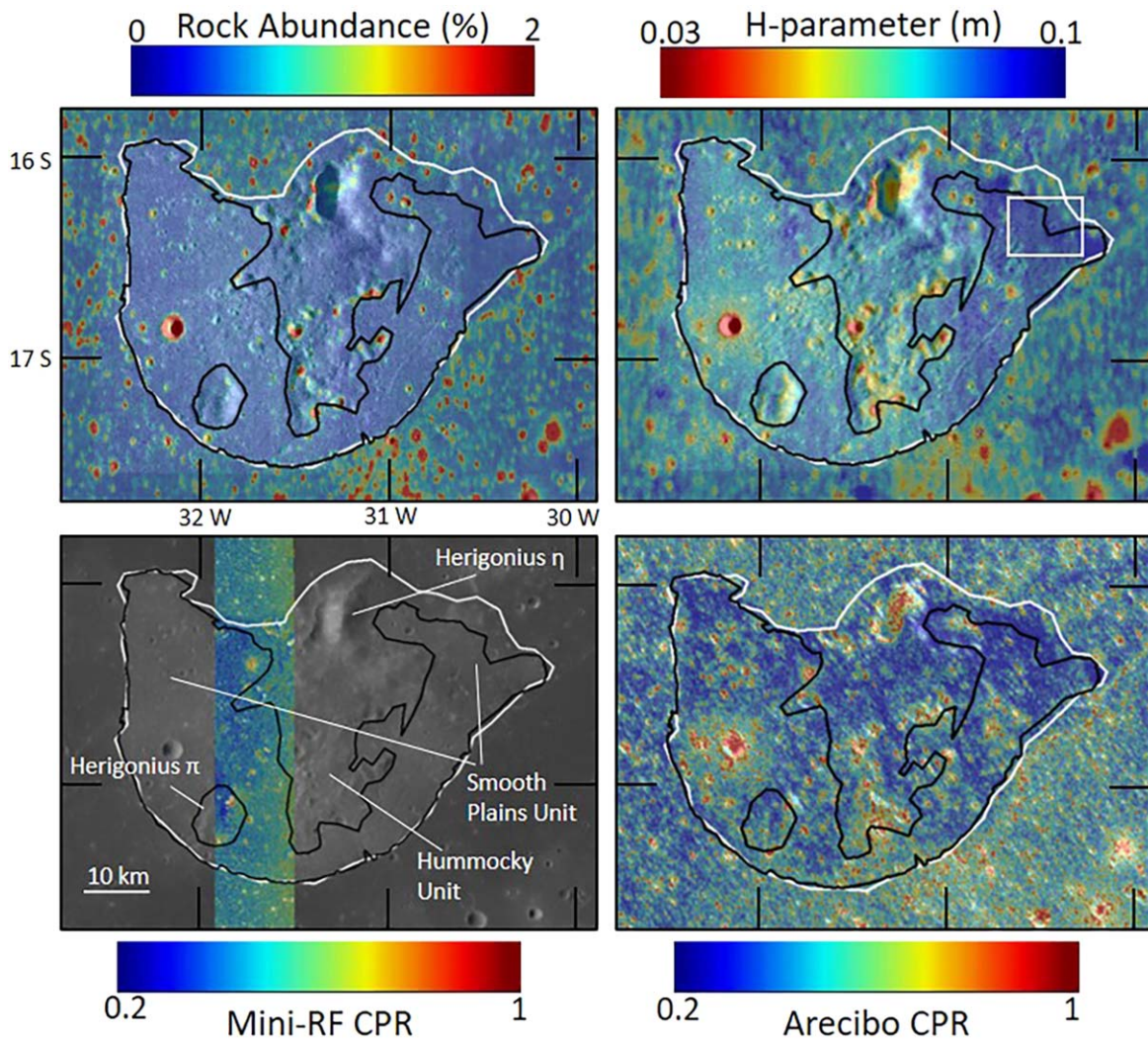
Figure 7. Rock abundance (top left), H-parameter (top right), Mini-RF CPR (bottom left), and Arecibo CPR (bottom right) maps covering Helmet. The white outlines represent the boundaries of the red spot locations determined by our study. The white box in the top-right image is the red spot location analyzed in Figure 15. Note that the color scale for the H-parameter map is inverted. The black outline represents the boundary between the Helmet Smooth Plains and Hummocky units, as defined by Meyer et al. (2020). The Diviner maps are overlain on LROC NAC image NAC_ROI_HELMET__LOA_E165S3289_5M. The Mini-RF CPR data are overlain on the S1 total backscatter data. The Arecibo CPR map is overlain on an Arecibo opposite-sense circular polarization image.
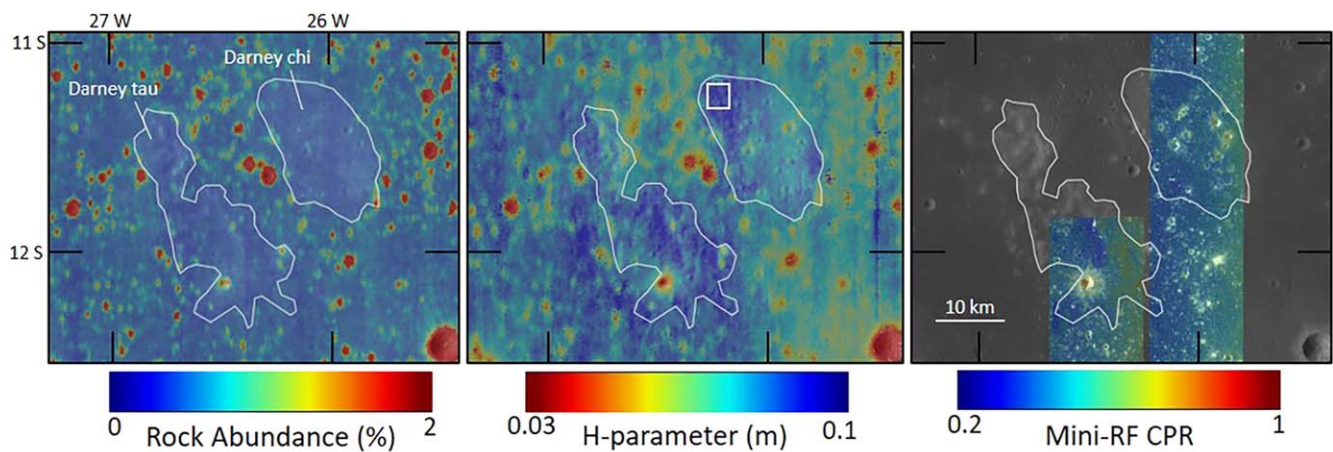

Figure 8. Rock abundance (left), H-parameter (center), and Mini-RF CPR (right) maps covering Darney-chi and -tau. The white outlines represent the boundaries of the red spot locations determined by our study. The white box in the center image is the red spot location analyzed in Figure 15. Note that the color scale for the H-parameter map is inverted. The maps are overlain on an LROC WAC global mosaic. The Mini-RF CPR data are overlain on the S1 total backscatter data.
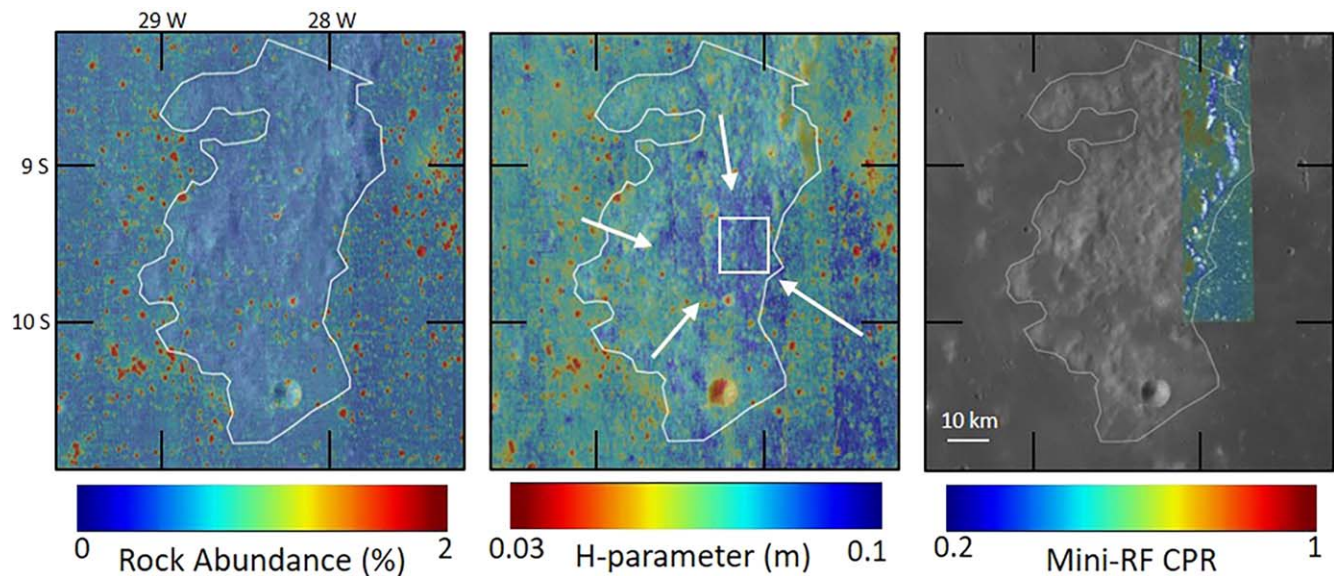
Figure 9. Rock abundance (left), H-parameter (center), and Mini-RF CPR (right) maps covering southern Montes Riphaeus. White arrows point out a region with relatively high H-parameter in the central part of Montes Riphaeus. The white outlines represent the boundaries of the red spot locations determined by our study. The white box in the center image is the red spot location analyzed in Figure 15. Note that the color scale for the H-parameter map is inverted. The maps are overlain on an LROC WAC global mosaic. The Mini-RF CPR data are overlain on the S1 total backscatter data.

amount of same-sense polarized light that is returned after bouncing off of randomly oriented cracks and edges from the rocks. Composition and incidence angle also affect the radar return and CPR, and must be accounted for when interpreting differences between the thermal IR and radar results. Rocks with high TiO_2 content are highly absorbing at radar wavelengths, resulting in lower backscatter and lower CPR (Campbell et al. 2010; Cahill et al. 2014). This is seen in the global S1 and CPR mosaics from Mini-RF (Cahill et al. 2014), where the basaltic maria appear radar dark (with low S1 return and low CPR), and the feldspathic highlands have higher S1 return and CPR. The red spots are generally low in TiO_2 content, however, and we have seen that in some situations they appear darker in both S1 and CPR than the surrounding maria. It is therefore unlikely that composition has a significant effect on the radar properties of the red spots; it is more likely that the presence of subsurface rocks is the primary mechanism affecting the radar backscatter and CPR values that we see. The effect of incidence angle on radar return is seen in some high-slope regions (e.g., the edges of the Gruithuisen domes). At low incidence angles, reflection is largely quasi-specular, and at high incidence angles diffuse scattering increases (Carter et al. 2011). Depending on the angle of the incident radar beam with respect to the surface topography, the CPR can appear anomalously high or low compared with nearby flat areas. For that reason, we must be careful when interpreting the results on high-slope areas, particularly with the silicic domes often having steep slopes.

We expect to see good agreement between the thermal IR and radar maps because both are generally affected by the presence of surface and subsurface rocky materials. However, disagreements do occur between the data sets (e.g., parts of the Gruithuisen domes and Helmet), and likely arise due to the different sensing depths of the instruments and their sensitivity to rocks of different sizes. Diviner senses changes in temperature up to the diurnal skin depth ($\sim$10 cm for regolith), but the S-band radar wavelengths observed by Mini-RF can penetrate >1 m into the surface. It is therefore possible that any

differences result from the depths and/or thicknesses of the various layers. For example, a near-surface fine-grained layer may appear as low thermal inertia in the H-parameter map, but if it is overlying a rockier layer, then it could appear as high CPR at S-band wavelengths. Conversely, a low CPR and a high thermal inertia could indicate an abundance of small rocks that contribute to the regolith thermal inertia but do not significantly scatter the S-band signals.

5.2. Material Properties of the Red Spots

In Section 4, we showed that each red spot displays slightly different RA, H-parameter, and CPR than the others. This is not unexpected because they exist in a number of geologic contexts (e.g., extrusive volcanic domes, basin structures, and exposures due to impact cratering). Some of the red spots contain areas of high RA associated with volcanic vents, depressions, or hummocky terrain (e.g., Figures 10, 11, and 12), and these areas generally also have high thermal inertia and high CPR, indicating that the terrain is rocky. Although the lifetime of rocks >1 m in diameter on the lunar surface is <1 Gyr (Ghent et al. 2014; Basilevsky et al. 2015), these areas likely remain rocky even after >3 Gyr because their rock population is replenished by mass wasting, which exposes fresh boulders when fine-grained material moves downslope (Nypaver et al. 2021). However, most of the red spots are generally less rocky (with fewer rocky impact craters) than the surrounding maria (Figure 13). This is expected because RA generally decreases with age (Cahill et al. 2014; Ghent et al. 2014), and in the highlands it is primarily large Copernican-age (<800 Ma) craters that have elevated rock concentration (Bandfield et al. 2011).

Red spots mostly lack uniform thermal inertia across the entirety of the features; however, we do observe small, localized areas of low thermal inertia (high H-parameter; Figure 15). Although a low RA, relative to the younger surrounding maria, at the red spots is not surprising because of their advanced age (>3.5 Gyr), the H-parameter generally
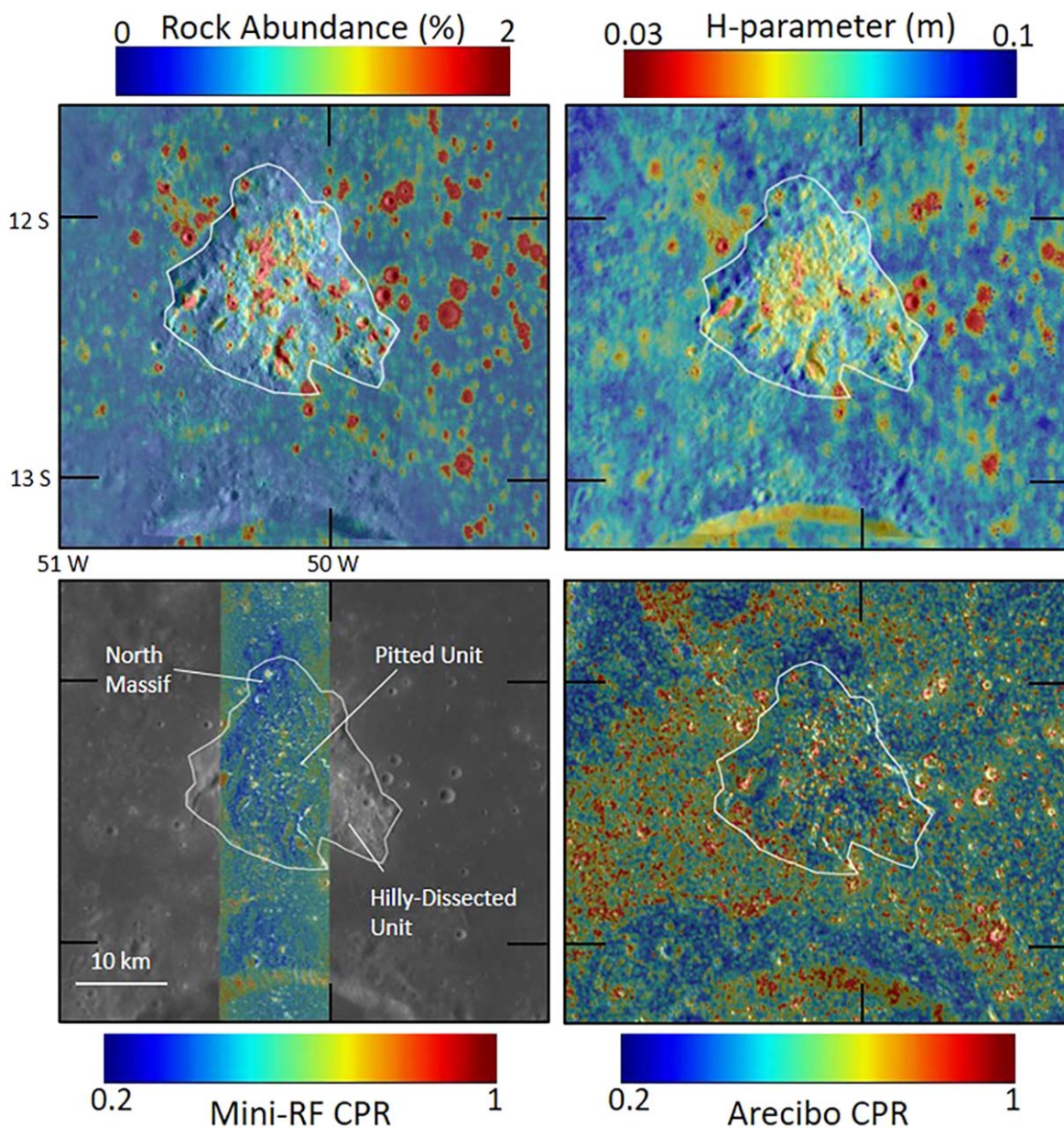
Figure 10. Rock abundance (top left), H-parameter (top right), Mini-RF CPR (bottom left), and Arecibo CPR (bottom right) maps covering Mons Hansteen. The white outlines represent the boundaries of the red spot locations determined by our study. Note that the color scale for the H-parameter map is inverted. The Diviner maps are overlain on LROC NAC image NAC_ROI_HANSTEENLOA_E124S3098_5M. The Mini-RF CPR data are overlain on the S1 total backscatter data. The Arecibo CPR map is overlain on an Arecibo opposite-sense circular polarization image.

blends in with the background after the first billion years (Hayne et al. 2017). Therefore, the observed spatial variability in the H-parameter is most likely due to a variability in the material properties.

The CPR of the red spots is generally consistent with the Diviner RA and H-parameter findings (i.e., low CPR where RA and thermal inertia values are low, and high CPR where RA and thermal inertia values are high). The reason for this connection is that the presence of rocks (both larger and smaller than the ~1 m size detected by the RA algorithm) is one of the main factors that contributes to the observed CPR (Carter et al. 2011; Cahill et al. 2014). The combination of these different parameters suggests that most of the red spots contain regions of relatively fine-grained or rock-poor regolith.

On the Moon, one context in which low RAs, thermal inertias, and CPRs are found is at regional pyroclastic deposits such as the Aristarchus Plateau and Sulpicius Gallus (Carter et al. 2009; Bandfield et al. 2011; Hayne et al. 2017). These pyroclastic deposits are proposed to contain relatively fine-grained material due to their formation by fire-fountaining eruptions (e.g., Gaddis et al. 1985). In many cases, the fine-grained deposits are seen to blanket the underlying terrain, resulting in a mantling of the low-lying areas while higher regions remain uncovered (Gaddis et al. 1985). Localized pyroclastic deposits, however, do vary in thermal inertia, some displaying high values (~0.08–0.09 m) and others low values (~0.05–0.06 m; Trang et al. 2017). This may result from post-eruption mixing with the surroundings via impact gardening or
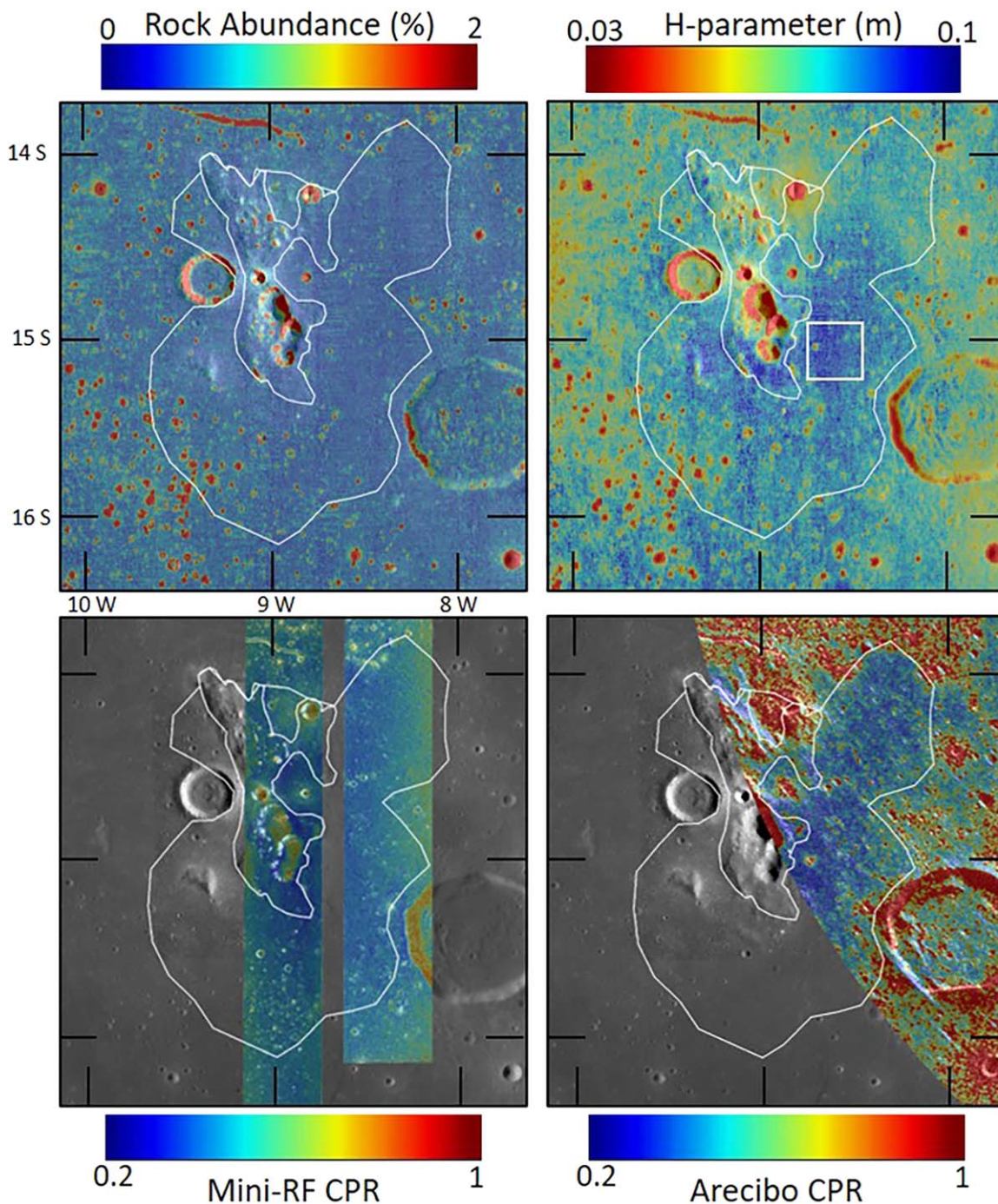
Figure 11. Rock abundance (top left), H-parameter (top right), Mini-RF CPR (bottom left), and Arecibo CPR (bottom right) maps covering the Lassell Massif. The white outlines represent the boundaries of the red spot locations determined by our study. The inner outline is the boundary of the massif, and the outer outline is the boundary of the reddish region from the Clementine color-ratio map. The white box in the top-right image is the red spot location analyzed in Figure 15. Note that the color scale for the H-parameter map is inverted. All maps are overlain on LROC NAC image NAC_ROI_LASSMASSLOA_E148S3508_5M. The Mini-RF CPR data are overlain on the S1 total backscatter data. The Arecibo CPR map is overlain on an Arecibo opposite-sense circular polarization image.

due to differences in the eruption type for localized pyroclastic deposits, which could form via intermittently explosive Vulcanian-style eruption (and can contain varying proportions of country rock) instead of fire-fountaining (Bennett et al. 2016).

We have observed that at least seven of the red spots have similar low RA, thermal inertia, and CPR values to those of the previously described pyroclastic deposits, suggesting that these red spots may also contain pyroclastic materials. Additional evidence for pyroclastic materials has been found using LROC NAC images (e.g., high reflectance indicating silicic glass, subdued morphologic features) at a number of red spots including Lassell Massif, Gruithuisen domes, Mons Hansteen, and CBVC (Ashley et al. 2016; Ivanov et al. 2016; Boyce et al. 2017; Clegg-Watkins et al. 2017), which supports the idea that pyroclastic materials may contribute to the observed material properties. However, not all red spots are emplaced in the same way, and mechanisms other than pyroclastic deposits exist that
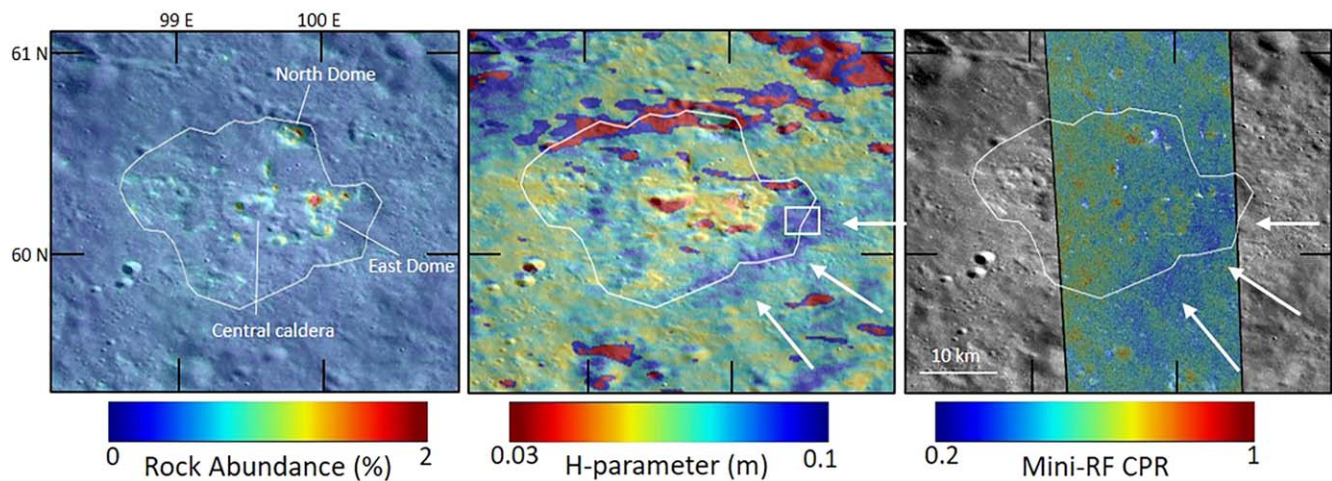
Figure 12. Rock abundance (left), H-parameter (center), and Mini-RF CPR (right) maps covering CBVC. The white outlines represent the boundaries of the red spot locations determined by our study. The white box in the center image is the red spot location analyzed in Figure 15. Note that the color scale for the H-parameter map is inverted. The southeastern part of CBVC and extending beyond the boundary (white arrows) is a high-albedo area that has low RA, high H-parameter, and low CPR. All maps are overlain on LROC NAC image NAC_ROI_COMPBELKLOE_E613N0993_5M. The Mini-RF CPR data are overlain on the S1 total backscatter data.

can result in fine-grained materials. In the following paragraphs, we describe these alternative mechanisms.

Other possible explanations for a high (0.08–0.10 m) H-parameter include the regolith having a lower thermal inertia due to a high regolith porosity, a lack of small rocks, and/or the rocks having a lower thermal inertia than other regions. These properties could result from the silicic composition of the lavas that formed some of the red spots, and/or the eruption dynamics that are associated with non-mare volcanism. For example, GRAIL gravity data indicate that the bulk crustal density of the Gruithuisen domes and Mons Hansteen is notably lower than surrounding regions, which Kiefer et al. (2016) attributed to an abundance of low-density felsic material that is relatively porous or vesicular. The gravity measurements from GRAIL represent the bulk crustal density (to a depth of ~tens of kilometers), which is significantly deeper than the near-surface density that can be inferred from Diviner measurements (~10 cm). However, this knowledge of the physical properties of the rocks that make up these regions may help us to interpret the RA and H-parameter data, noting especially that density is the main cause for spatial variability in thermal inertia on the Moon.

The rockiness and porosity of a target surface can be affected by eruption dynamics and composition, and are known to affect impact cratering and rock excavation (e.g., Williams et al. 2022). When an impact occurs in a porous target, much of the energy goes toward driving material downward (i.e., "crushing" the porosity), and less energy goes toward shearing and ejecting material from the crater cavity (Housen & Holsapple 2011, 2012). This results in less rock being excavated for a high-porosity target than for a lower-porosity target, meaning any impact craters into a high-porosity surface would have lower RA than would be expected for a similar impact into a less-porous target. Boyce et al. (2018) noted that the surface of the Mairan "Middle" dome contained relatively few rocky impact craters, and suggested that the surface of the dome could have been composed of rubbly, porous volcanic breccia materials similar to those seen at terrestrial silicic domes (Duffield et al. 1995). When subsequent impacts would have occurred into this volcanic breccia surface, the result would be

more of the energy from impacts going toward crushing the rubble into finer grains rather than excavating the rock underneath (Housen & Holsapple 2011, 2012). If some red spots were initially covered by a layer of rubbly, porous volcanic breccia, then impacts into their surfaces would likely not excavate large amounts of rock but crush the rubble into finer grains, thereby contributing toward the low RA, low thermal inertia, and lack of subsurface rocks that we see at a number of the red spots.

Another possibility is that the felsic materials that formed some of the red spots were mechanically weaker (and possibly more vesicular or glassy) than the denser and coherent basaltic lava flows, resulting in higher breakdown rates from micrometeorite impacts. Impact experiments using quartz and feldspar as targets were found to be comminuted more easily than basaltic targets (Cintala & Horz 1992). Similarly, thermal cycling experiments found that rock type and mineralogy had an effect on microflaking, cracking, and comminution of the samples, with microflaking occurring more often on lunar anorthosite breccia and cracking being more common on a basaltic eucrite (Patzek & Rüsch 2022). If the rocks that formed the felsic red spots tended to break down into a regolith that is somewhat finer-grained and rock-poor compared with surrounding mare regions, then that may contribute toward the lower RAs, higher H-parameters, and lower CPRs that we see at the red spots.

Alternatively, it is possible that some of the red spots were mantled by a fine-grained ejecta layer from a large crater or basin-forming impact. Ejecta materials from Imbrium, Orientale, and earlier basin impacts are thought to have modified the lunar surface prior to the emplacement of the majority of mare basalts (Meyer et al. 2020). The geologic unit associated with basin formation materials is known as the lunar light plains, with ~70% of light plains attributed to the Imbrium and Orientale events (Meyer et al. 2020). Similarly, low radar returns were observed in the Montes Jura region of the Moon in both 3.8 and 70 cm Arecibo radar data sets, which Thompson et al. (2006) proposed were due to overlapping ejecta deposits from the Sinus Iridum and Plato craters. The ejecta deposits in the Montes Jura region are likely several meters thick, and are
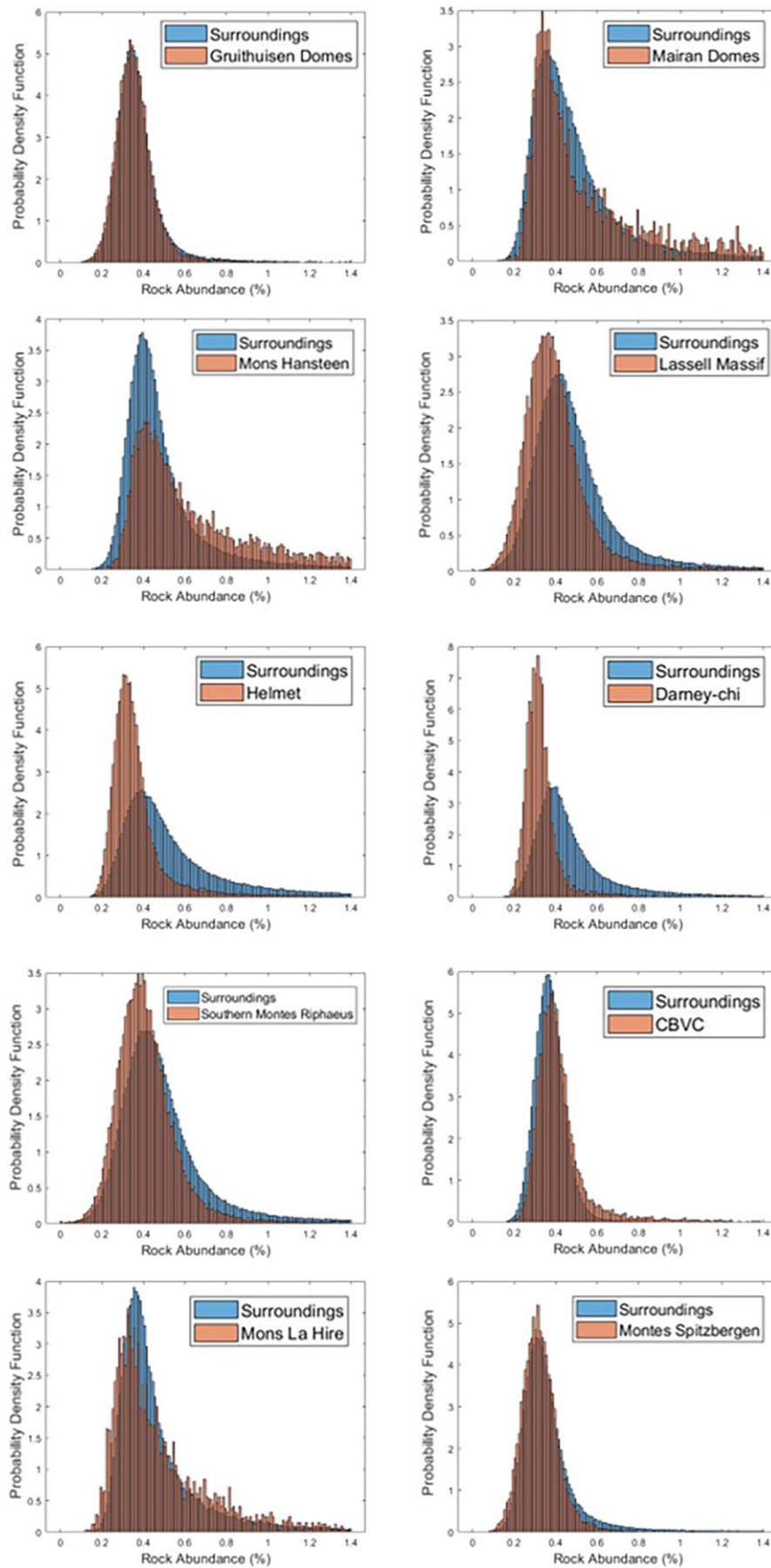
Figure 13. Histograms of rock abundance for areas within the red spot boundaries (white polygons in Figures 3–12; orange histograms) and outside the red spot boundaries (blue histograms). Red spots generally have similar or slightly lower RA than nearby regions.
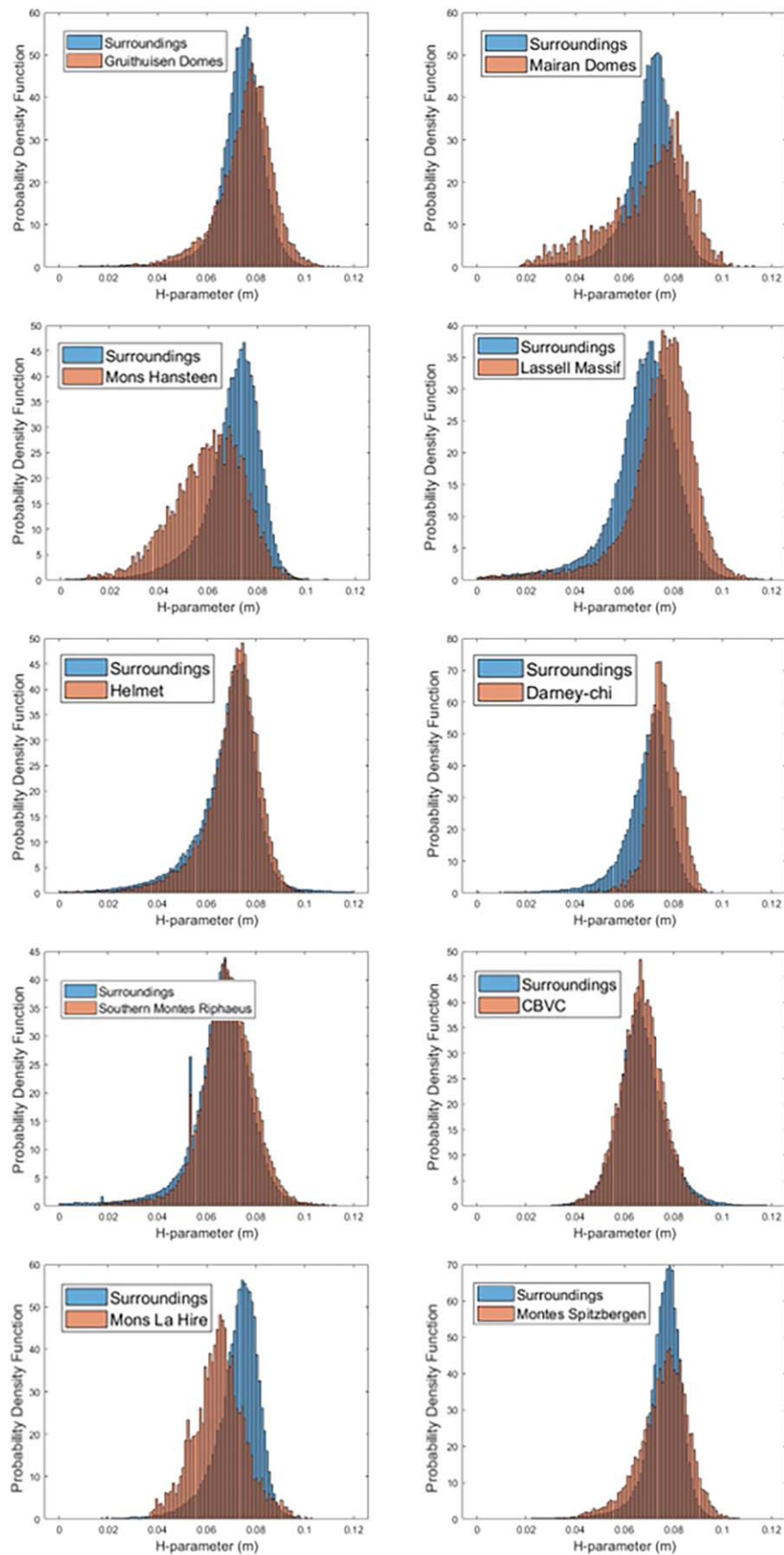
Figure 14. Histograms of the H-parameter for areas within the red spot boundaries (white polygons in Figures 3–12; orange histograms) and outside the red spot boundaries (blue histograms).
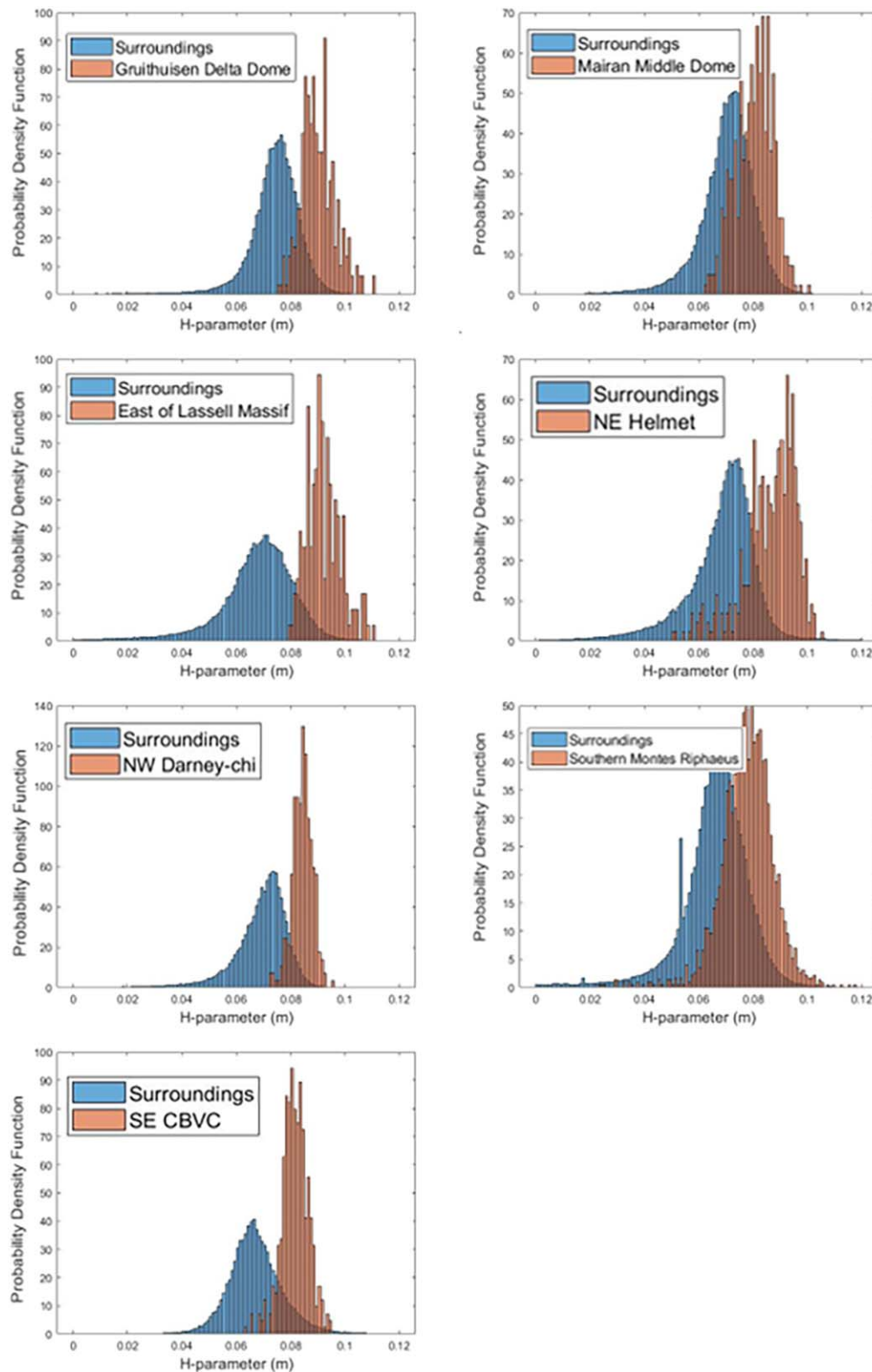
Figure 15. Histograms of H-parameter for selected areas within the red spot boundaries (white boxes in Figures 3, 4, 7, 8, 9, 11, 12; orange histograms) and areas outside the red spot boundaries (blue histograms). Selected regions within a number of red spots have a noticeably higher H-parameter than nearby mare regolith.

depleted in rocks >10 cm (Thompson et al. 2006). If any similar deposits exist at the red spots, they would likely have low RA, high H-parameter, and low CPR.

Some combination of each of these hypotheses (pyroclastic material, porosity, rock strength, ejecta deposits) likely contributes to the differences in thermophysical properties; therefore, it is necessary to investigate each red spot separately in its own context. In the following sections, we focus on individual sites and discuss the likely mechanisms that led to the material properties that we observe.
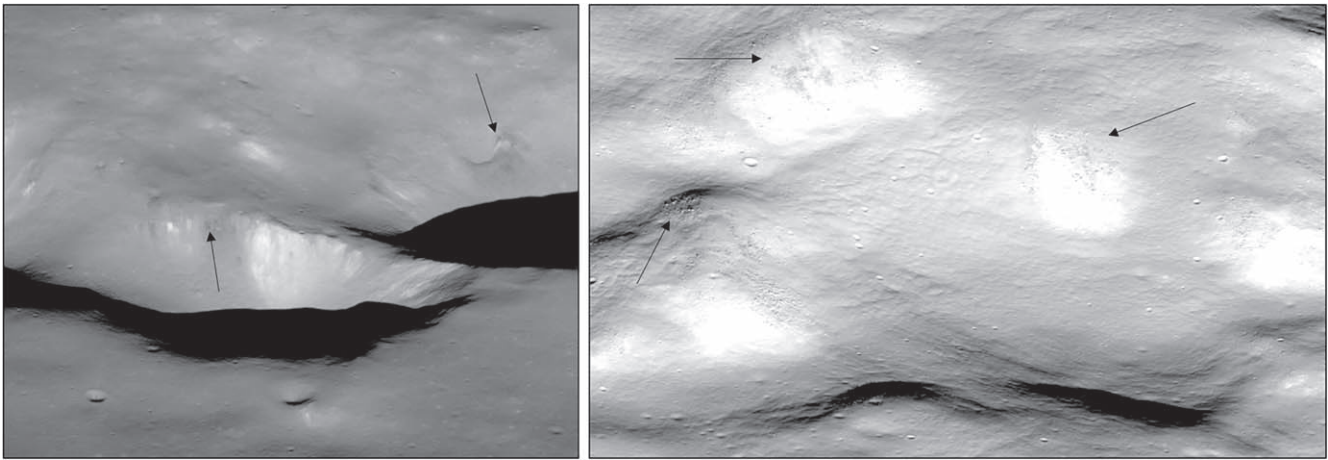
Figure 16. Evidence for pyroclastic material at the Lassell Massif and Mons Hansteen red spots. Left: oblique view of the irregular craters G and K on the Lassell Massif. Black arrows point out exposures of low albedo material that may be related to pyroclastic deposits, as described in Ashley et al. (2016). Right: oblique view of the Pitted Unit on Mons Hansteen. Black arrows point out rock exposures at higher topography areas of the Pitted Unit. The higher thermal inertia rocky exposures may be obscuring any low thermal inertia materials that preferentially accumulate in the lower-lying areas on top of Mons Hansteen. Images are from LROC NAC mosaics M1108311369 and M1154506530LR, respectively.

5.3. CBVC, Mons Hansteen, and the Lassell Massif: Signatures of Pyroclastic Material

Unlike many other red spots, CBVC has been previously shown to display signatures of pyroclastic material. For example, the southeastern side of CBVC shows evidence for explosive pyroclastic volcanism in a number of data sets, including high reflectance in LROC images showing similarities with a glassy silicic analog (Clegg-Watkins et al. 2017), relatively low CPR values suggesting a surface layer of fine-grained materials (Bhattacharya et al. 2013; Chauhan et al. 2015), and elevated thorium values (14–26 ppm) extending eastward from CBVC indicating pyroclastic dispersal (Jolliff et al. 2011; Wilson et al. 2015). These studies proposed that this area was subject to an explosive eruption (possibly associated with caldera collapse) that blanketed the area to the east with pyroclastic, ash-like materials. An ash flow would blanket the low-lying areas with fine-grained material, resulting in lower thermal inertia in the low-lying areas than at higher elevations. Our observations support these findings, as the H-parameter data (Figure 12) show that the high-albedo deposit extending toward the southeast beyond the boundary of CBVC has low thermal inertia (H-parameter ∼0.08–0.09 m). The locations of low thermal inertia additionally show good agreement with the areas of relatively low CPR in the Mini-RF map.

Previous work has also suggested that the Lassell Massif displays signatures of pyroclastic material (Ashley et al. 2016; Carter et al. 2017b). Carter et al. (2017b) found that the area surrounding Lassell Massif was radar dark with low CPR in Earth-based S-band radar images, indicating the presence of pyroclastic material in the surface or near-subsurface. This radar dark area coincides with a diffuse reddish feature in the Clementine color-ratio map (Figure 1) extending outward from the two large irregular craters (possibly calderas) on the massif (Lassell G and K), providing further evidence for volcanic emplacement. Ashley et al. (2016) additionally noted low-reflectance material exposed by impact craters in and around the Lassell Massif and by mass wasting in the irregular craters Lassell G and K (Figure 16), supporting the existence of pyroclastic material. We see relatively low CPR surrounding

the massif to the south and east in the Mini-RF and Arecibo maps, which correlates reasonably well with the regions of low RA (∼0.3%) and high H-parameter (∼0.09–0.10 m; Figure 11). This, along with the central massif topped by possible calderas, suggests that the material properties we see are most likely the result of the pyroclastic material.

Boyce et al. (2017) found that the morphologic features of Mons Hansteen were consistent with pyroclastic mantling, similar to those seen at CBVC (e.g., bench craters indicating layers with different coherency and blanketing by volcanic ash-type material; Boyce et al. 2017). The Diviner data, however, show that the top of Mons Hansteen is fairly rocky (∼1%–2%) and has high thermal inertia (H-parameter ∼0.04–0.05 m; Figure 10), which is in contrast to typical pyroclastic deposits. In fact, even a 2 cm thick layer of fine-grained material above coherent rock would significantly lower the surface temperature relative to pure rock (Elder et al. 2017), which would result in low RA values. The fact that Mons Hansteen does not display low thermal inertia likely has to do with the rocky nature of the Pitted and Hilly Dissected Units and the likelihood that any pyroclastic material would have settled into lower-lying areas on top of the dome. These units contain elongated pits and troughs that have been suggested to be volcanic vents (Boyce et al. 2017). The rims and slopes of these vents are rocky and have high thermal inertia (Figure 16), and are likely to obscure any potential low thermal inertia materials that could be blanketing portions of the top of the dome. Therefore, even if significant amounts of low thermal inertia materials accumulated in low-lying areas, the scattering and emission of infrared radiation from the surrounding slopes could significantly elevate the temperatures on the floor of the depression (Powell et al. 2023). However, the evidence for fine-grained material is more obvious in the Mini-RF and Arecibo radar data, where we see relatively low CPR across the dome in the lower-lying regions that are less rocky and pitted (Figure 10). We do see relatively low RA and low thermal inertia values in some of these locations as well (e.g., on the North Massif and parts of the Hilly Dissected Unit). This is consistent with the presence of a mantle of fine-grained (possibly pyroclastic) material like that suggested by Boyce et al. (2017); however, it could also be

related to the accumulation of fine-grained material in lower regions due to mass wasting.

CBVC, Mons Hansteen, and the Lassell Massif all show signs of mantling by fine-grained material in visible wavelength images, and the presence of pyroclastic material has been detailed by previous studies (Chauhan et al. 2015; Ashley et al. 2016; Boyce et al. 2017; Clegg-Watkins et al. 2017). The good agreement that we see between the different data sets in this study (i.e., low RA, thermal inertia, and CPR) at CBVC and the region surrounding Lassell Massif's irregular craters G and K supports previous suggestions of pyroclastic material at those locations. At Mons Hansteen, the presence of pyroclastic material is less clear in the Diviner data sets than at CBVC and Lassell Massif, though some areas (e.g., the North Massif and parts of the Hilly Dissected Unit) have low RA and low CPR, which could be consistent with pyroclastic material.

5.4. Helmet, Darney-chi and -tau, and Southern Montes Riphaeus: Pre-mare Highlands in the Cognitum Region

The Helmet feature has low RA throughout the smooth plains unit that covers most of the western and eastern parts of the feature, except for a small number of large craters that show high RA inside and around their rims (Figure 7). The central hummocky unit contains a number of rocky exposures and impact craters, but has generally lower RA than surrounding maria. The eastern/northeastern part of Helmet has lower thermal inertia than the surrounding mare, while the western smooth plains unit and much of the hummocky unit have similar thermal inertia to surrounding mare. The relatively low CPR seen in the Mini-RF and Earth-based radar data sets along with the Diviner RA and H-parameter results suggest that a rock-poor layer exists within the top ∼1 m throughout Helmet, though it is most noticeable in the northeastern section. This would be consistent with pyroclastic material; however, Bruno et al. (1991) argued that there is no morphologic evidence for pyroclastic mantling. A more likely explanation is that parts of the feature (in particular, the light plains unit) are covered by relatively rock-poor ejecta materials, as Meyer et al. (2020) showed that on the global scale light plains units are typically related to basin ejecta. However, the hummocky unit of Helmet also shows generally low CPR, suggesting that some other explanation (e.g., its composition) could contribute to the presence of fine-grained materials there. Based on UV-visible spectra, Bruno et al. (1991) determined that the hummocky unit and light plains unit are compositionally distinct from each other, and that the two units are compositionally distinct from the surrounding mare. And although the Helmet feature is not silicic in composition (Glotch et al. 2010), the finding that it is compositionally distinct from the mare suggests that the preferential comminution into finer-grained particles due to its felsic composition could play some role in its material properties as well.

Darney-chi and -tau are both rock-poor compared to the surrounding maria, and parts of the features display a low thermal inertia fines component (Figure 8). In the Mini-RF S1 return map (Figure 17) of Darney-chi, we see high return related to crater cavities and ejecta in the central part of the feature. The northwestern part of the feature, however, shows low S1 return and lacks rocky impact craters. The radar dark area of Darney-chi also shows low thermal inertia (H-parameter ∼0.09 m), while the rockier central part has higher thermal inertia (likely due to the greater amount of subsurface rocks in

the crater ejecta deposits). No clear signs of pyroclastic material have been found at Darney-chi, though it possible that the low thermal inertias and CPRs seen at northwestern Darney-chi are the result of previously undiscovered pyroclastic deposits. However, Darney-chi is classified as a light plains unit (Meyer et al. 2020), similar to that found at Helmet. This suggests that a mantling by rock-poor basin ejecta could explain the material properties of the feature. It must be noted, however, that a volcanic origin has not been ruled out for Darney-chi and other light plains units (Wagner et al. 2010; Meyer et al. 2020). It is therefore possible that the material properties of Darney-chi are related to the preferential comminution into fine-grained particles due to the weakness of the felsic target rock at those locations compared with surrounding maria.

Southern Montes Riphaeus has fewer rocky craters than surrounding maria, and a portion of it has a slightly higher H-parameter (∼0.08 m; Figures 9 and 15). However, the intercrater mare plains to the east of the red spot appear to have similar H-parameter to the high-H part of Montes Riphaeus. Due to the poor coverage from Mini-RF and lack of coverage from Earth-based radar data sets, the subsurface rock content of Montes Riphaeus is unclear. However, the low RA (∼0.4%) and slightly higher H-parameter in some locations suggests that relatively fine-grained material is present in some places.

The red spots described in this section (Helmet, Darney-chi and -tau, southern Montes Riphaeus) are all located in the Mare Cognitum region, and likely represent remnant pre-mare highlands-type material excavated in the Cognitum basin-forming impact (Wood & Head 1975). These red spots may or may not be associated with extrusive volcanism, and although spectrally red, are not highly silicic like some of the other red spots (Glotch et al. 2010). The low RA, thermal inertia, and CPR locations within these features are therefore unlikely to be related to pyroclastic deposits. The most likely explanation is that the red material existed in the region prior to the Cognitum basin-forming event, and that either the Cognitum impact or some other nearby large impact occurred and deposited the rock-poor red ejecta in this region. Subsequent mare volcanism would have buried much of the ejecta, but the topographically higher areas could have been embayed but not covered by the basalts. We must note, however, that the felsic composition of these red spots could also have played a role in their material properties. Although Helmet, Darney-chi, and southern Montes Riphaeus are not highly silicic (Glotch et al. 2010), they are felsic in comparison with the surrounding mare and may have preferentially comminuted into finer grains as a result of this.

5.5. Gruithuisen and Mairan: Extrusive Silicic Domes

Ivanov et al. (2016) suggested that pyroclastic material is present at the Gruithuisen domes, noting fine-grained exposures of both light- and dark-colored material on the wall of an impact crater on the Gruithuisen Gamma dome (Figure 18). They suggested that the light-colored materials originated from outcrops of high-albedo (possibly silicic) boulders and that the dark-colored materials are related to either glassy pyroclastic particles or dark-colored pumices (Ivanov et al. 2016). This particular area does not display the lower thermal inertia characteristic of fine-grained pyroclastic material, but instead has slightly higher thermal inertia than the surroundings (H-parameter = 0.048 m), likely due to a greater abundance of rocks mixed in with the regolith from the excavation stage when the impact occurred. The possibility that pyroclastic
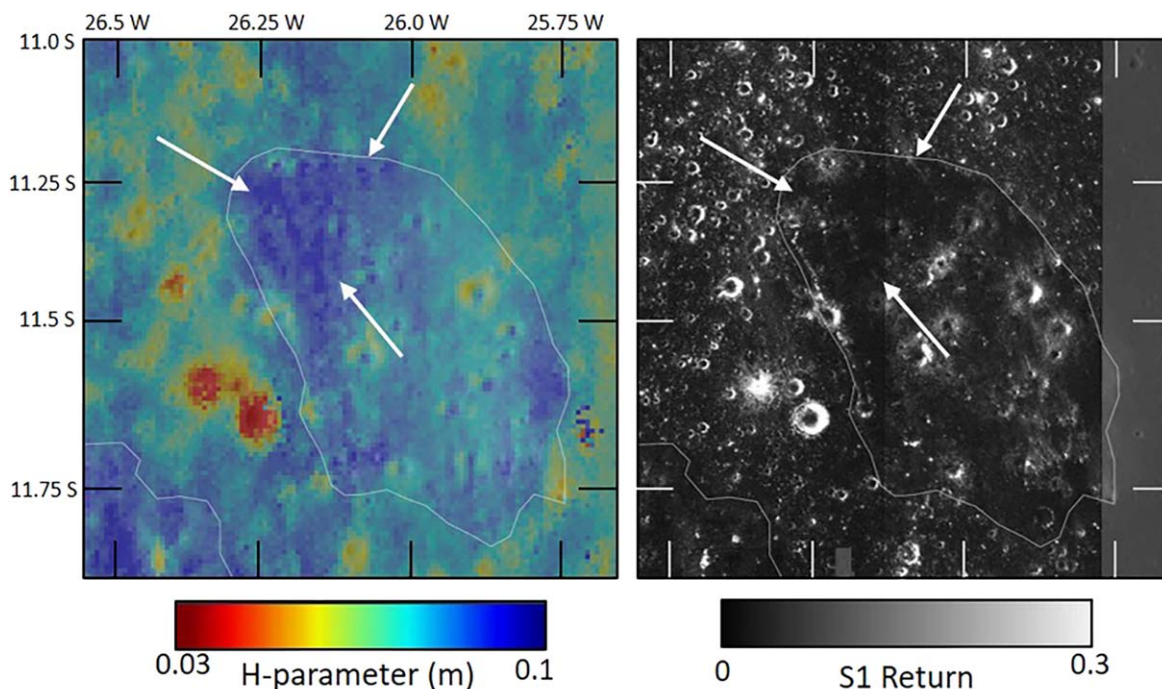
Figure 17. Diviner H-parameter map (left) and Mini-RF S1 Return map (right) for Darney-chi. White arrows show the radar-dark and low thermal inertia area in northwestern Darney-chi.
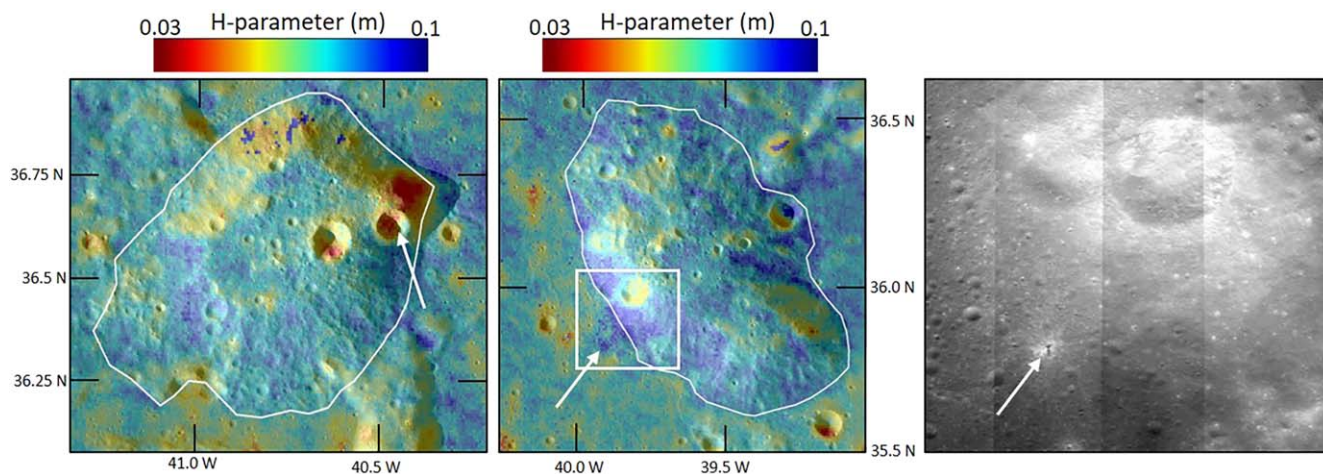

Figure 18. Close-up views of craters on the Gruithuisen domes. Left: Diviner H-parameter map of the Gruithuisen Gamma dome. The white arrow points out the crater where Ivanov et al. (2016) found evidence for possible pyroclastic material. Center: Diviner H-parameter map of the Gruithuisen Delta dome. The white arrow points out a small area of high H-parameter on the maria just west of the dome. Right: LROC NAC images (M155499183L and M155499183R) showing the ∼120 m diameter fresh crater west of the Delta dome that is likely associated with the cold spot seen in the H-parameter map. Note that the H-parameter color scale is inverted. The Diviner maps are overlain on LROC NAC image NAC_ROI_GRUITHSNLOB_E362N3197_5M.

materials may be present in the walls of this impact crater and not noticeably apparent across the surface of the domes suggests, if present, pyroclastic layers could exist at depth.

The Gruithuisen domes display low thermal inertia values (H-parameter ∼0.08–0.10 m) only in certain places (e.g., the southwest-facing slope of the Delta dome), but appear to have low RA (∼0.3%–0.4%) everywhere except for at the few larger (>2 km) craters on each dome (Figure 3). The southwest-facing slope of the Delta dome displays a noticeably high H-parameter (Figure 18), and also contains a relatively large (2.2 km) crater that has exposed underlying materials from within the dome. The crater itself displays slightly higher thermal inertia (H-parameter ∼0.055 m) than typical regolith (likely due to rocks excavated by the impact), but the

surrounding dome slopes display noticeably lower thermal inertia (H-parameter ∼0.09 m). If the Delta dome does have lower bulk density than typical regions as the GRAIL results suggest (Kiefer et al. 2016) and/or contains buried pyroclastic material, then it is possible that the crater ejected relatively fine-grained material or that few rocks were ejected from the crater cavity, resulting in the observed low thermal inertias.

It must be noted that the southwest-facing walls of the Delta dome are relatively steep (∼20°–30°), and some amount of mass wasting should have occurred. In most cases, we expect that any overlying fines would gradually slide off, exposing rockier surfaces underneath. However, the slopes are expected to be lower than the angle of repose (∼31°.5–34°; Kokelaar et al. 2017), so it is possible that only small amounts of mass

wasting occurred, and the slopes still retained some of the low thermal inertia fine-grained material.

Another explanation is that the observed material properties are a result of the highly silicic nature of the dome (i.e., the relative weakness of the silicic target rock made comminution by small impacts more effective, resulting in a finer-grained and less rocky regolith). Alternatively, the rocks that made up the dome at this location could have been primarily composed of the rubbly and porous volcanic breccia that Boyce et al. (2018) proposed for the Mairan "Middle" dome. Subsequent impacts would then result in the preferential crushing and comminution of the surface rocks rather than excavation of underlying rock.

An interesting feature to note is that a small region of high H-parameter is seen on the maria just west of the Delta dome. Upon closer examination through LROC NAC images, this site appears to be the location of a small (∼120 m diameter) fresh crater (Figure 18), and the H-parameter anomaly here is likely due to the presence of a cold spot associated with the crater (e.g., Bandfield et al. 2014; Williams et al. 2018). Cold spots (named as such due to their low nighttime temperatures within ∼10–100 crater radii) likely result from a decompaction of the regolith within the upper few centimeters (Bandfield et al. 2014), leading to anomalously high H-parameter values. Although this cold spot is close to the Delta dome (∼2 km at the closest point), we do not expect it to be the cause of the low-thermal inertia region on the southwest-facing slope of the dome. This is because based on the crater size, we can estimate the maximum radial distance of the cold spot surface to be ∼1.7 km, using the scaling relationship from Bandfield et al. (2014).

The Mairan "Middle" dome has low RA (∼0.45%) and a slightly higher H-parameter (0.08 m) than surrounding maria (Figure 4), which suggests a relatively fine-grained regolith. This is consistent with the Boyce et al. (2018) porous volcanic breccia hypothesis. Interestingly, the CPR of the "Middle" dome is relatively high (∼0.75–1.0) compared with the highlands to the east (∼0.2–0.5), although some small areas of relatively low CPR exist in the central and eastern parts of the dome. This difference in CPR is perhaps not surprising, however, as the highlands to the east of the Mairan domes are suggested to be mantled by relatively rock-poor ejecta from the Sinus Iridum impact that occurred prior to the emplacement of the domes (Thompson et al. 2006). The relatively high CPR values that we see on the "Middle" dome are particularly noticeable at specific locations on the north, west, and south parts of the feature, which contain a number of irregularly shaped pits (Boyce et al. 2018). Upon closer inspection, these high-CPR areas also have slightly elevated RA and low H-parameter compared to the central and eastern parts of the dome (Figure 4), indicating good agreement between the thermal IR and radar data sets. Despite the evidence for fine-grained material at the Mairan "Middle" dome, we see little evidence at the Mairan "T" and "South" domes, which display high RA, low H-parameter, and high CPR (Figure 4).

The Gruithuisen and Mairan domes are examples of extrusive silicic volcanic features, with morphologies similar to terrestrial silicic domes (Head et al. 1978). Given the similarities with terrestrial silicic domes, the Boyce et al. (2018) hypothesis that the surface of the Mairan "Middle" Dome could have been covered by a rubbly, porous volcanic breccia and preferentially crushed into finer grains by impacts

is a plausible explanation for our findings at both the Mairan and Gruithuisen domes. However, we cannot rule out that the presence of pyroclastic material or that the preferential comminution of the silicic target material into fine grains could have resulted in the material properties we observe at the domes. The upcoming Lunar-VISE CLPS payload delivery (Donaldson-Hanna et al. 2023) will land on one of the Gruithuisen domes, and its in situ measurements will reveal some of the material properties of the rocks and regolith, which will improve our understanding of the Diviner remote sensing data.

5.6. Mons La Hire and Montes Spitzbergen: Imbrium Basin-related Structures

Most of Mons La Hire has low RA (∼0.3%), and we see only a few small areas with a slightly higher H-parameter than surrounding maria (Figure 5). We additionally see relatively high CPR across most of the feature in the Arecibo radar map, in particular at the crater in the eastern part. Using the Clementine color-ratio map, the reddest area of Mons La Hire is observed in a diffuse area surrounding this crater, while the rocky south-facing slope is blue likely due to immature material being exposed by mass wasting (Figure 19). The red material may have been buried and subsequently exposed by the impact crater here. The relatively high CPR values here are likely caused by a greater abundance of subsurface rocks in the proximal ejecta of the crater. Mons La Hire forms part of the Imbrium basin inner ring, and is likely not volcanic in nature. The low RA across much of the feature is likely due to its advanced age (∼3.85 Gyr; Stoffler & Ryder 2001). However, most of the feature (except for a few small areas of possible mass-wasted material) does not have low thermal inertia or low CPR, so Mons La Hire does not appear to contain abundant fine-grained material.

Similar to Mons La Hire, Montes Spitzbergen is part of the Imbrium basin inner ring and is also not likely a volcanic landform. It has a low RA (∼0.3%) across most of the feature and contains some small areas with relatively high H-parameter (Figure 6). The peaks show relatively high CPR in the Arecibo map, while the lower-lying areas have lower CPR. The lower-lying areas appear red in the Clementine color-ratio map, and most of the peaks are blue (Figure 19). The blue colors likely represent relatively immature highlands-type material exposed due to mass wasting on the slopes. Mass-wasted material may then accumulate in the lower-lying areas, resulting in the low CPR values we see in some locations at the base of the peaks. However, similar to Mons La Hire, the existence of fine-grained material is less clear than we see at some of the other red spots.

5.7. Summary

At the red spot locations that previously have been suggested to contain pyroclastic material (CBVC, Mons Hansteen, and the Lassell Massif), we generally see low RA, thermal inertia, and CPR values. The agreement between these different data sets indicates an abundance of fine-grained material, which strengthens the argument for pyroclastic material at these locations. At other red spots where pyroclastic material has not been suggested (Helmet, Darney-chi and -tau, southern Montes Riphaeus) or where evidence for pyroclastic volcanism has been suggested but is less clear (Gruithuisen domes, Mairan
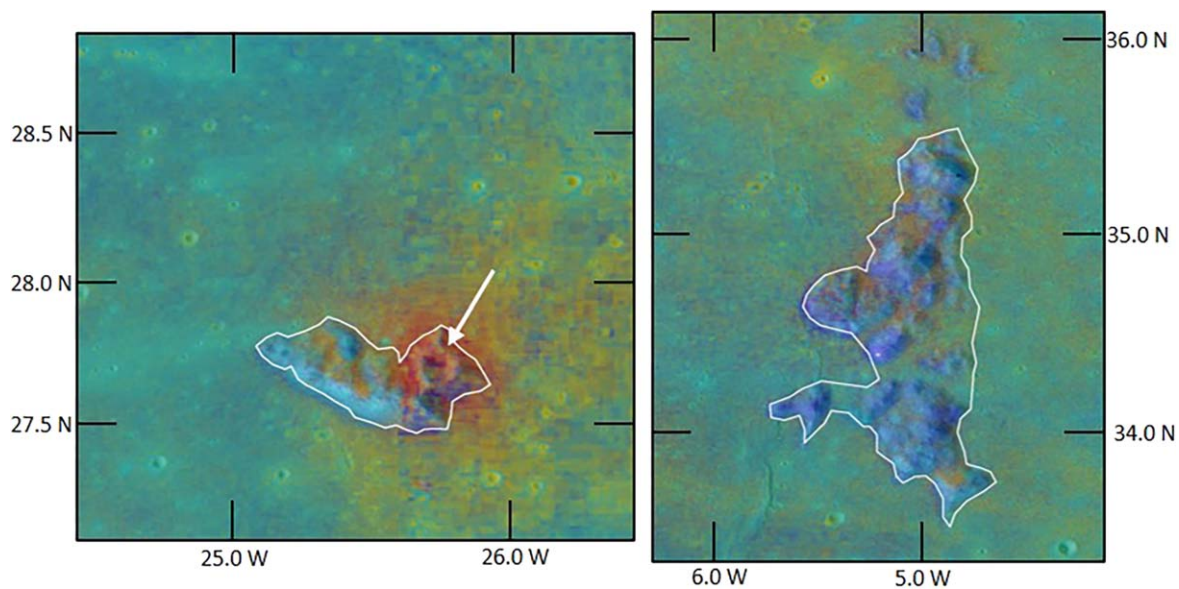
Figure 19. Clementine color-ratio maps of Mons La Hire (left) and Montes Spitzbergen (right). The reddest area of Mons La Hire is mostly surrounding a crater on the east side of the feature, and the reddest areas of Montes Spitzbergen are found in the lower-lying areas surrounding the peaks.

domes), we also see localized regions of low RA, thermal inertia, and CPR. This suggests that fine-grained material exists at these locations that may be unrelated to pyroclastic volcanism. At the Helmet, Darney-chi, and southern Montes Riphaeus red spots, the fine-grained material likely results from mantling by rock-poor ejecta deposits or from the preferential comminution into finer grains due to their felsic composition. At the Gruithuisen and Mairan domes, it is more likely that the fine-grained material results from the physical properties of the silicic target rocks (i.e., preferential comminution due to their silicic composition or the rubbly, porous nature of the possible volcanic breccias that covered the domes). At Mons La Hire and Montes Spitzbergen, we see low RA values but do not see evidence for fine-grained material in the H-parameter and CPR maps, which may result from mass wasting exposing rocky underlying material at these features.

6. Conclusions

Red spots are compositionally unique features on the Moon that are proposed to be formed by non-mare volcanism, and are therefore of interest as potential landing sites for future missions. We have investigated the material properties of 10 lunar red spots using thermal infrared data from LRO Diviner and radar data from LRO Mini-RF and Arecibo Observatory. We found that all of the red spots we investigated have similar or lower RA than their surroundings, and at least seven contain localized regions where the fines component shows lower thermal inertia than typical regolith. This result is derived from an albedo map that we produced using data from the Diviner solar channels. Previous results from Hayne et al. (2017) using the LOLA albedo map did not fully resolve the red spots and therefore resulted in an overestimation of the H-parameter. We also observed that at least five of the red spots (CBVC, Mairan "Middle" dome, Lassell Massif, Helmet, and Darney-chi) show low radar backscatter and low CPR in the same locations that show low RA and thermal inertia. These findings suggest that these locations within the red spots contain primarily fine-grained and rock-poor material in the top ~1 m of the surface.

Some red spots (CBVC, Lassell Massif, Mons Hansteen) display low RA, low regolith thermal inertia, and low CPR in the same locations where previous studies have found evidence of pyroclastic material using LROC NAC images and radar data sets. Pyroclastic material is typically fine-grained and rock-poor, and our interpretation of thermophysical and radar observations supports the notion of pyroclastic material at these red spots. Pyroclastic material has also been suggested to occur at the Gruithuisen domes, exposed within the wall of an impact crater. However, our Diviner and Mini-RF results do not support this claim, as we see relatively high thermal inertia and CPR at the impact crater where pyroclastic material has been suggested. Along the southwest side of the Gruithuisen Delta dome, however, is an impact crater surrounded by low thermal inertia material, which may indicate that fine-grained material has been excavated there.

Red spots in the Mare Cognitum area (Helmet, Darney-chi and -tau, and southern Montes Riphaeus) are associated with the Cognitum or Humorum basin-forming impacts, and may or may not have been formed by extrusive volcanism. However, our results suggest that fine-grained, rock-poor material is present at these red spots in localized regions, which could be explained by the presence of pyroclastic material. Alternatively, the presence of fine-grained material at these red spots may be evidence of mantling by rock-poor ejecta from a large impact or basin-forming event prior to the eruption of mare basalts. Subsequent mare volcanism would then have buried much of the ejecta, leaving only the topographically higher regions exposed.

Our findings may also suggest that the regolith at certain red spot locations (e.g., the Gruithuisen and Mairan domes) has higher porosity or finer grain size, not due to explosive eruption, but instead as a result of the nature of silicic materials, such as rock strength or the vesicularity/porosity of small rocks. Many of the red spots were formed from highly silicic materials with lower density than basalts, and some studies have suggested that they could have been highly vesicular or glassy, which would lower thermal inertia. Furthermore, it is possible that impact comminution functions differently on

silicic rocks than on basaltic rocks, and that the silicic rocks at red spots could have preferentially broken down into finer-grained material through impact bombardment. Boyce et al. (2018) proposed that some red spots (e.g., Mairan "Middle" dome) were initially covered by a surface layer of rubbly, porous volcanic breccia, and when impacts occurred in this material, those impacts were less effective at excavating rock and more effective at breaking the rubble down into finer-grained particles. Both of these could explain the low RA, low thermal inertia, and low CPR values that we see. Each red spot exists in a slightly different geologic context, and it could be a combination of pyroclastic material, porosity, and rock strength that causes the observed differences in material properties.

Acknowledgments

ORCID iDs

Benjamin D Byron ● https://orcid.org/0000-0003-4435-0347
Catherine M. Elder ● https://orcid.org/0000-0002-9993-8861
Timothy D. Glotch ● https://orcid.org/0000-0002-8187-3609
Paul O. Hayne ● https://orcid.org/0000-0003-4399-0449

References

Ashley, J. W., Robinson, M. S., Stopar, J. D., et al. 2016, Icar, 273, 248
Bandfield, J. L., Cahill, J. T., Carter, L. M., et al. 2017, Icar, 283, 282
Bandfield, J. L., Ghent, R. R., Vasavada, A. R., et al. 2011, JGRE, 116, E00H02
Bandfield, J. L., Song, E., Hayne, P. O., et al. 2014, Icar, 231, 221
Basilevsky, A., Head, J., Horz, F., & Ramsley, K. 2015, P&SS, 117, 312
Bennett, K. A., Horgan, B. H., Gaddis, L. R., et al. 2016, Icar, 273, 296
Bhattacharya, S., Saran, S., Dagar, A., et al. 2013, CSci, 105, 685, https://www.currentscience.ac.in/Volumes/105/05/0685.pdf
Boyce, J. M., Giguere, T., Mouginis-Mark, P., et al. 2018, P&SS, 162, 62
Boyce, J. M., Giguere, T. A., Hawke, B. R., et al. 2017, Icar, 283, 254
Bruno, B. C., Lucey, P. G., & Hawke, B. R. 1991, LPSC, 21, 405
Cahill, J. T., Thomson, B. J., Patterson, G. W., et al. 2014, Icar, 243, 173
Campbell, B. A. 2002, Radar Remote Sensing of Planetary Surfaces (Cambridge: Cambridge Univ. Press)
Campbell, B. A. 2012, JGRE, 117, E06008
Campbell, B. A., Carter, L. M., Campbell, D. B., et al. 2010, Icar, 208, 565
Carter, L. M., Campbell, B. A., Hawke, B. R., et al. 2009, JGRE, 114, E11004
Carter, L. M., Campbell, B. A., Neish, C. D., et al. 2017a, ITGRS, 55, 1915
Carter, L. M., Campbell, D. B., & Campbell, B. A. 2011, IEEEP, 99, 770
Carter, L. M., Petro, N. E., & Campbell, B. A. 2017b, LPSC, 1964, 1736
Chauhan, M., Bhattacharya, S., Saran, S., et al. 2015, Icar, 253, 115
Cintala, M. J., & Horz, F. 1992, Metic, 27, 395
Clegg-Watkins, R. N., Jolliff, B. L., Watkins, M. J., et al. 2017, Icar, 285, 169
Donaldson-Hanna, K., Benavente, J., Bennet, K., et al. 2023, LPSC, 54, 2152

Duffield, W. A., Richter, D. H., & Priest, S. S. 1995, Geologic map of the Taylor Creek rhyolite and adjacent rocks, Catron and Sierra counties, New Mexico IMAP 2399, USGS, https://pubs.usgs.gov/imap/2399/report.pdf
Elder, C. M., Hayne, P. O., Bandfield, J. L., et al. 2017, Icar, 290, 224
Gaddis, L. R., Pieters, C. M., & Hawke, B. R. 1985, Icar, 61, 461
Ghent, R. R., Carter, L. M., & Bandfield, J. L. 2016, Icar, 273, 182
Ghent, R. R., Hayne, P. O., Bandfield, J. L., et al. 2014, Geo, 42, 1059
Glotch, T. D., Hagerty, J. J., Lucey, P. G., et al. 2011, GeoRL, 38, L21204
Glotch, T. D., Jawin, E. R., Greenhagen, B. T., et al. 2021, PSJ, 2, 136
Glotch, T. D., Lucey, P. G., Bandfield, J. L., et al. 2010, Sci, 329, 1510
Gullikson, A. L., Hagerty, J. J., Reid, M. R., et al. 2016, AmMin, 101, 2312
Hagerty, J. J., Lawrence, D. J., Hawke, B. R., et al. 2006, JGRE, 111, E06002
Hawke, B. R., Lawrence, D. J., Gillis, J. J., et al. 2003, LPSC, 34, 1545
Hayne, P. O., & Aharonson, O. 2015, JGRE, 120, 1567
Hayne, P. O., Bandfield, J. L., Siegler, M. A., et al. 2017, JGRE, 122, 2371
Head, J. W., Hess, P. C., & McCord, T. B. 1978, LPSC, 9, 488
Head, J. W., III, & McCord, T. B. 1978, Sci, 199, 1433
Hess, P. C., Rutherford, M. J., Guillemette, R. N., et al. 1975, LPSC, 6, 895
Hiesinger, H., Head, J. W., III, Wolf, U., Jaumann, R., & Neukum, G. 2011, in Recent Advances and Current Research Issues in Lunar Stratigraphy, Vol. 477, ed. W. A. Ambrose & D. A. Williams (McLean, VA: GSA)
Hildreth, W. 1981, JGR, 86, 10153
Housen, K. R., & Holsapple, K. A. 2011, Icar, 211, 856
Housen, K. R., & Holsapple, K. A. 2012, Icar, 219, 297
Ivanov, M. A., Head, J. W., & Bystrov, A. 2016, Icar, 273, 262
Jolliff, B. L., Wiseman, S. A., Lawrence, S. J., et al. 2011, NatGe, 4, 566
Kiefer, W. S., Taylor, G. J., Andrews-Hanna, J. C., et al. 2016, LPSC, 47, 1722
Kokelaar, B. P., Bahia, R. S., Joy, K. H., et al. 2017, JGRE, 122, 1893
Kusuma, K. N., Sebastian, N., & Murty, S. V. S. 2012, P&SS, 67, 46
Lawrence, D. J., Elphic, R. C., Feldman, W. C., et al. 2003, JGRE, 108, 5102
McEwen, A. S., & Robinson, M. S. 1997, AdSpR, 19, 1523
Meyer, H. M., Denevi, B. W., Robinson, M. S., & Boyd, A. K. 2020, JGRE, 125, e06073
Neal, C. R., & Taylor, L. A. 1989, LPSC, 19, 209
Nypaver, C. A., Thomson, B. J., Fassett, C. I., et al. 2021, JGRE, 126, e06897
Paige, D. A., Foote, M. C., Greenhagen, B. T., et al. 2010, SSRv, 150, 125
Patzek, M., & Rüsch, O. 2022, JGRE, 127, e2022JE007306
Powell, T. M., Horvath, T., Lopez Robles, V., et al. 2022, LPSC, 53, 2274
Powell, T. M., Horvath, T., Robles, V. L., et al. 2023, JGRE, 128, e2022JE007532
Qiu, D., Ye, M., Yan, J., et al. 2022, JGRE, 127, e2022JE007289
Raney, R. K., Spudis, P. D., Bussey, B., et al. 2010, IEEEP, 99, 808
Ravi, S., Till, C. B., & Robinson, M. S. 2020, LPSC, 51, 1145
Ravi, S., Till, C. B., & Robinson, M. S. 2022, AGUFM, 2022, U25B–0497
Roedder, E., & Weiblen, P. W. 1970, Geotimes, 15, 10
Roedder, E., & Weiblen, P. W. 1971, LPSC, 2, 507
Roedder, E., & Weiblen, P. W. 1972, LPSC, 3, 251
Roy, A., Mallik, A., Barnes, J., et al. 2023, LPSC, 54, 2751
Scholten, F., Oberst, J., Matz, K. D., et al. 2012, JGRE, 117, E00H17
Shirley, K. A., Zanetti, M., Jolliff, B. V., et al. 2016, Icar, 273, 214
Shkuratov, Y., Kaydash, V., Rohacheva, L., et al. 2016, Icar, 272, 125
Stöffler, D., & Ryder, G. 2001, SSRv, 96, 9
Thompson, T. W., Campbell, B. A., Ghent, R. R., et al. 2006, JGRE, 111, E06S14
Trang, D., Gillis-Davis, J. J., Lemelin, M., et al. 2017, Icar, 283, 232
Vasavada, A. R., Bandfield, J. L., Greenhagen, B. T., et al. 2012, JGRE, 117, E00H18
Wagner, R., Head, J. W., III, Wolf, U., et al. 2002, JGRE, 107, 14
Wagner, R., Head, J. W., III, Wolf, U., et al. 2010, JGRE, 115, E06015
Whitaker, E. A. 1972, Moon, 4, 348
Williams, J. P., Bandfield, J. L., Paige, D. A., et al. 2018, JGRE, 123, 2380
Williams, J. P., Paige, D. A., Greenhagen, B. T., et al. 2017, Icar, 283, 300
Williams, J. P., Pathare, A. V., Costello, E. S., et al. 2022, JGRE, 127, e07131
Wilson, J. T., Eke, V. R., Massey, R. J., et al. 2015, JGRE, 120, 92
Wood, C. A., & Head, J. W. 1975, Origins of Mare Basalts and their Implications for Lunar Evolution, Vol. 234 (Houston, TX: Lunar Science Inst.), 189
Yu, S., & Fa, W. 2016, P&SS, 124, 48